Laser systems for the cooling of calcium monofluoride molecules

Bachelor's thesis
presented by

Ekkehard Noah Steinmacher

August 18, 2022

Examiner: Dr. Tim Langen

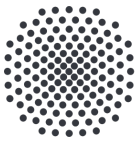

Universität Stuttgart

5. Physikalisches Institut
Universität Stuttgart

Declaration of Authorship

I hereby certify that this thesis is entirely my own work except where otherwise indicated. Passages and ideas from other sources have been clearly indicated. Neither this nor a similar work has been presented to an examination committee. The electronic and printed versions of this thesis are identical.

Stuttgart, August 18, 2022 Ekkehard Noah Steinmacher

Zusammenfassung

Ultrakalte Moleküle bieten eine bahnbrechende Plattform in der Atomphysik, die Anwendungen in den Bereichen der ultrapräzisen Atomuhren, der Quantensimulationen und Quantenberechnungen, der Präzisionsmessungen, sowie der kalten und ultrakalten Chemie hat. Um diese Plattform, insbesondere im Gebiet der Quantensimulationen mit langreichweitigen dipolaren Wechselwirkungen, weiter auszuweiten, wird die Erzeugung eines molekularen Bose-Einstein Kondensats (BEC) mit Kalziumfluorid (CaF) Molekülen angestrebt. Die Manipulation der Bewegung und der inneren Zustände dieser Moleküle durch wechselwirken mit Lasern spielt eine entscheidende Rolle bei der Erzeugung eines BEC.

In dieser Arbeit werden der Kühllaser, den $X^2\Sigma^+(\nu = 0) \longrightarrow A^2\Pi_{1/2}(\nu = 0)$ Übergang von CaF treibend und der erste Rückpumplaser, den $X^2\Sigma^+(\nu = 1) \longrightarrow A^2\Pi_{1/2}(\nu = 0)$ Übergang treibend aufgebaut und charakterisiert. Beide Lasersysteme sind ein Teil der magneto-optischen Falle (MOT). Sie bestehen jeweils aus einem Diodenlaser, der als „Seed“-Laser für einen Faserverstärker dient, sowie einer Frequenzverdopplungseinheit. Der Kühllaser emittiert Licht bei 606,3 nm mit Leistungen bis zu 1,6 W und der erste Rückpumplaser Licht bei 628,6 nm mit Leistungen bis zu 2,1 W. Darüber hinaus werden sie für eine Zeitspanne von über 25 Minuten mittels eines Fabry-Perot-Interferometers frequenzstabilisiert. Des Weiteren wird ebenfalls ein Dipolfallenlaser aufgebaut und charakterisiert, welcher Licht bei 1064 nm mit bis zu 46,5 W an Leistung emittiert und eine Leistungsstabilität von ±0,16 % über zwei Stunden aufweist. Ein Leistungsstabilisierungsschema für diesen Laser wird ebenfalls vorgeschlagen. Die MOT-Laser und der bereits zuvor konstruierte Verlangsamungslaser bilden das Rückgrat unseres neuen Experiments und ebnen nun den Weg für kommende Experimente zur Verlangsamung und Kühlung des Molekülstrahls.

Abstract

Ultracold molecules provide a groundbreaking platform in atomic physics with applications in the fields of ultraprecise atomic clocks, quantum simulation and computing, precision measurements and cold and ultracold chemistry. Bose-Einstein condensates (BECs) of dipolar molecules such as calcium monofluoride (CaF) can further extend the capabilities for simulating quantum systems with long-range dipolar interactions. The manipulation of the motion and internal states of these molecules through the interaction with lasers play a crucial part in the creation of a BEC.

In this thesis, the cooler operating on the $X^2\Sigma^+(\nu = 0) \longrightarrow A^2\Pi_{1/2}(\nu = 0)$ transition of CaF and the first repumper operating on the $X^2\Sigma^+(\nu = 1) \longrightarrow A^2\Pi_{1/2}(\nu = 0)$ transition are set up and characterized. Both of these laser systems are used in the magneto-optical trap (MOT) which captures and holds the molecules. Each laser system consists of a diode laser acting as a seed laser for a fiber amplifier and a frequency-doubling unit. The cooler emits light at 606.3 nm with powers up to 1.6 W. The first repumper emits light at 628.6 nm with powers up to 2.1 W. Moreover, both lasers are locked on a scanning transfer cavity for a time span over 25 minutes. Also in this thesis, a dipole trap laser is set up and characterized. It emits light at 1064 nm with powers up to 46.5 W and has a power stability of $\pm 0.16\,\%$ over two hours. A power stabilization scheme for this laser also is proposed. In combination with the previously constructed slowing laser, the MOT lasers of this thesis form the backbone of our new experiment, paving the way for upcoming new CaF molecular beam slowing and cooling experiments.

Contents

List of Figures

List of Tables

1 Introduction

The concept of laser cooling of atoms was first conceived in the 1970s by Arthur Ashkin [1,2], as well as by the group of Theodor W. Hänsch and Arthur L. Schawlow [3] and by the group of David J. Wineland and Hans G. Dehmelt [4]. They proposed that the repeated absorption and spontaneous emission of resonant photons could slow the movement of an atom, which in an atom ensemble could even lead to temperatures in the microkelvin range [5]. In the following years, physicists used the newly developed concepts to experimentally cool sodium atoms to these temperatures [6]. As laser cooling techniques improved, they thought, that they would be limited by the recoil velocities emerging from many light-matter scattering processes of a single atom [7]. These recoils act like a heating, that balance the cooling at low temperatures and therefore an equilibrium should set in at the Doppler temperature. However, in experiments temperatures lower than the Doppler temperature were soon found [7, 8]. Only later these sub-Doppler cooling techniques, like creating bright molasses for utilizing a Sisyphus cooling mechanism [9, 10] or applying evaporative cooling [11] were understood. This allowed the groups of Carl E. Wieman, Eric A. Cornell and Wolfgang Ketterle in 1995 to observe a new state of matter in the ultracold region [12, 13], the Bose-Einstein condensate, which had been proposed 70 years before [14, 15]. This exotic state of matter is characterized by an ensemble of particles all occupying the same ground state, forming a macroscopic quantum mechanical state [16].

Laser cooling is an essential step on the road to Bose-Einstein condensation. In order to achieve this, a closed cooling cycle is important so that scattering processes of the atom with photons can take place without the atom leaving the two level system. In contrast to atoms, laser cooling of molecules was long thought impossible, because of their complicated energy structure [10]. There are additional rotational and vibrational energy states in molecules because they have more degrees of freedom [17]. When trying to laser cool molecules as done for atoms, this would lead to molecules decaying into many different rotational and vibrational states which are not addressed by the cooling lasers. However, in 2004 a class of molecules with favorable decay properties was identified [18]. This has lead to successful demonstrations of Doppler cooling of molecules [19], sub-Doppler cooling of diatomic [20, 21] and even polyatomic molecules [22], dipole trapping of molecules [23], magneto-optical trapping of molecules [24–26] and the manipulation of molecules in optical tweezers [27].

Building on this progress, the goal in our group is to realize a Bose-Einstein condensate of laser cooled molecules. Later on, we would like to explore self-bound dipolar droplets and supersolids in molecular Bose-Einstein condensates [28].

Our molecule of choice for this goal is calcium monofluoride (CaF). This choice is motivated by CaF's low mass, large electric dipole moment as well as an energy level structure which is well suitable for molecular laser cooling. In particular, CaF features several transitions with highly diagonal Franck-Condon factors [10].

The goal of this thesis is the setup and characterization of the cooler and first repumper required to address the $X^2\Sigma^+ \longrightarrow A^2\Pi_{1/2}$ transition of CaF, which will be used for the magneto-optical trap. Moreover, this thesis characterizes a dipole trap laser that will allow trapping of the molecules in a conservative dipole trap potential after laser cooling.

2 Theory

2.1 Laser cooling of molecules

Ever since the the first demonstration of laser cooling of atoms [5], the technique has been the workhorse for experiments involving ultracold atoms and ultracold molecules. In laser cooling, photons are absorbed and spontaneously emitted by an atom or a molecule [10].

2.1.1 Doppler cooling in a two level system

The scattering force Laser cooling reduces the temperature T of a cloud of atoms or molecules. Modeled as an ideal gas, the temperature is directly correlated to their mean velocity $\bar{v}$ by $T = \frac{m \cdot \bar{v}^2}{3 \cdot k_\mathrm{B}}$, where m is the mass of a single atom or molecule and k_B is the Boltzmann constant [16]. Therefore, slowing the atoms or molecules in an ensemble directly causes a reduction of the temperature of the ensemble.

But before looking at the case of laser cooling molecules, let us simplify the task by first considering atoms [10]. In general, atoms in a thermal cloud have a mean velocity of roughly 300 m/s to 600 m/s at room temperature, but for cold and ultracold atom experiments the temperatures should be in the microkelvin to nanokelvin range, corresponding to 20 mm/s or less [8, 13].

For simplicity, let us consider an atom as a two level system with the ground state and the excited state separated by an energy gap ΔE. If the atom is in the ground state, it can absorb a photon with frequency $\omega = \frac{\Delta E}{\hbar}$, $\hbar$ being the reduced Planck's constant. This absorption transfers the atom into the excited state. The photon has a momentum $\hbar\mathbf{k}$ and momentum is conserved during the absorption. So, the absorption of the photon changes the momentum of the atom. Spontaneous decay from the excited state back into the ground state emits a photon in a random direction. For a large number of scattering events, the decay processes does not transfer momentum to the atom. Each scattering event changes the velocity of a single atom by its recoil velocity Δv which is typically of the order $\Delta v \approx 0.03\,\mathrm{m/s}$. So, typically many thousands of scattering events are needed to slow an atom of the ensemble towards standstill. For this, the photons have to propagate antiparallel to the atom's velocity.

Doppler cooling In order to cool a particle ensemble, there must be a force opposed to the direction of motion of a particle, no matter which direction the particle moves in. Thus,

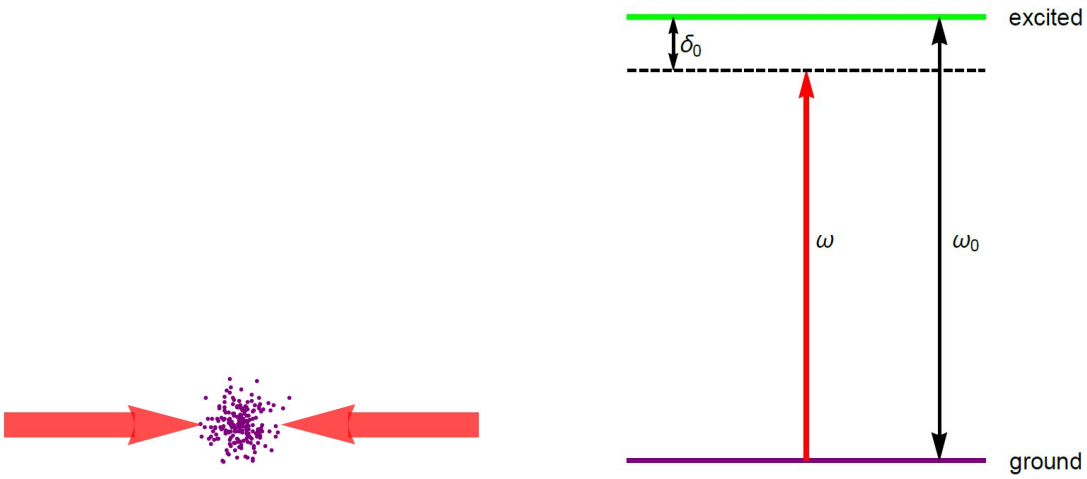

Figure 2.1: Doppler cooling in 1D. (a) Two red-detuned counterpropagating laser beams interact with the atoms or molecules. (b) The laser beam frequency ω is smaller than the transition frequency ω_0 by the detuning δ_0. Figures taken from [10].

first of all, all spatial directions have to be covered. Therefore, a typical setup involves one laser beam from each direction. This is sketched in 1D in Figure 2.1a. In 3D this involves a total of six beams. Second, a mechanism has to be implemented so that the absorption of photons counterpropagating to the particle's direction of movement is favored. Only then the particle will be decelerated. This mechanism is based on the Doppler effect [3, 10].

If a moving particle interacts with an electromagnetic wave, the frequency of the electromagnetic wave observed by the particle increases if the particle is counterpropagating with respect to the wave. Therefore, if the frequency of the light is red-detuned by the detuning δ_0, then the Doppler shift causes the counterpropagating laser beam to be more resonant to the transition frequency. Vice versa, the copropagating laser beam is less resonant. So, independent of the particle's velocity, the particle is more likely to scatter a counterpropagating photon than a copropagating photon. Hence a reduction of the particles velocity is achieved. Usually δ_0 is order of the natural line width Γ of the excited state. Figure 2.1b shows Doppler cooling in one dimension and an oversimplified energy level scheme of an atom, a two-level system.

Figure 2.2 shows the acceleration of the atom as a function of its velocity. The resulting effective force is velocity dependent and drives the velocity towards zero velocity.

However, the atom's velocity will not reach zero with Doppler cooling. As the velocity tends to zero the absorption from both beams becomes equally likely and the individual random momentum kicks from each photon emission become important. The momentum

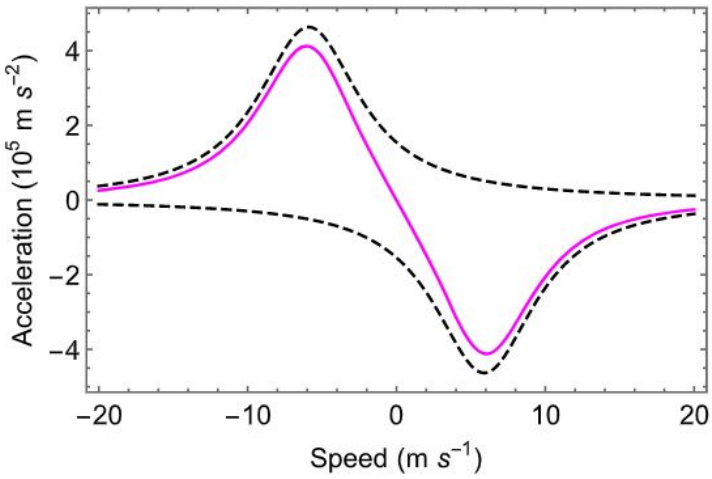

Figure 2.2: The cooling force acting on an atom depends on its velocity. The dashed lines show the accelerations of the individual beams. The solid line is their sum and thus proportional to the total force. Figure taken from [10].

kicks by scattering photons with momentum $\hbar\mathbf{k}$ act as a heating mechanism, preventing the atom from reaching zero velocity. An equilibrium between cooling and heating mechanism will be reached at the Doppler temperature T_D. It is given by

$$T_\mathrm{D} = \frac{\hbar\Gamma}{2k_\mathrm{B}} \tag{2.1.1}$$

and is the minimal temperature which can be achieved through Doppler cooling in a two-level system. Usually Doppler temperatures are in the microkelvin range. This is too high for Bose-Einstein condensation, for which temperatures in the nanokelvin range are required. Lower temperatures are realized through sub-Doppler cooling techniques like Sisyphus cooling or evaporative cooling [10, 11].

In evaporative cooling, atoms or molecules are transfered into conservative potentials like that of an optical dipole trap [11]. By lowering the trap depth, the most energetic particles are removed, while the remaining ones rethermalize by collisions. In this way, temperatures in the nanokelvin range can be reached, facilitating the formation of a Bose-Einstein condensate [12, 13].

2.1.2 Energy structure of calcium monofluoride

Real atoms and molecules are many-level systems, bringing cooling challenges like dark states and many possible transitions. It is thus very important to gain a precise knowledge of the energy levels.

Molecular state notation The ground state of a molecules is labeled X and the first and second electronically excited states are labeled A and B [17]. Since the spherical symmetry in a diatomic molecule is broken, the electronic orbital and spin angular momenta L and S are not good quantum numbers anymore. However, their projections onto the internuclear axis (z-axis) $\mathbf{L_z} = \pm\Lambda\hbar$ and $\mathbf{S_z} = \hbar\Sigma$ are good quantum numbers. The states with the values $\Lambda = 0, 1, 2, ...$ are labeled Σ, Π, Δ, ... The projection Σ has the discrete values $\Sigma = S, S-1, ..., -S$ with S being the spin of the electron. The quantum number $\Omega = |\Lambda+\Sigma|$ is the total electronic angular momenta. The molecular state notation is given by

$$^{2S+1}\Lambda_{\Omega}. \tag{2.1.2}$$

Sometimes Ω is omitted and replaced by the parity (u or g) and the symmetry (+ or -) in the molecular state notation. The ground state in CaF is symmetrical with respect to symmetry along the internuclear axis and it has $S = \frac{1}{2}$ and $\Lambda = 0$. So the CaF ground state is noted as $X^2\Sigma^+$ [29].

Energy structure The energy structure of molecules is very complicated compared to that of atoms. This is because molecules have electronic energy levels, fine structure and hyperfine structure levels, just like as atoms, and also have additional vibrational and rotational energy levels [17].

Diatomic molecules such as calcium monofluoride can be approximated as a non-rigid rotor. The rotational energy in this case is given by

$$E_{\text{rot}} = \frac{\hbar^2}{2\mu R_{\text{e}}^2}N(N+1) - \frac{\hbar^4}{2k\mu^2 R_{\text{e}}^6}N^2(N+1)^2. \tag{2.1.3}$$

Here μ is the reduced mass, R_{e} the distance between the nuclei in equilibrium, k the spring constant and N the rotational quantum number [17]. In spectroscopy it is more common to express the rotational energy as

$$E_{\text{rot}} = hc \cdot \left(B \cdot N(N+1) - D \cdot N^2(N+1)^2\right) \quad \text{with} \tag{2.1.4}$$

$$B = \frac{h}{8\pi^2 c\Theta} \quad \text{and} \tag{2.1.5}$$

$$D = \frac{\hbar^3}{4\pi k\Theta^2 R_{\text{e}}^2 c}. \tag{2.1.6}$$

Here Θ is the moment of inertia of the molecule and B and D are rotational constants.

The vibrational interaction is modeled through the Morse potential. It can be approximated as a harmonic potential to first order. So, the first term of the vibrational energy is analogous to the energy of the quantum mechanical harmonic oscillator. The vibrational energy up to second order is given by [17]

$$E_{\text{vib}} = \hbar\omega_{\text{e}}\left(\nu + \frac{1}{2}\right) - \hbar\omega_{\text{e}}\chi_{\text{e}}\left(\nu + \frac{1}{2}\right)^2. \tag{2.1.7}$$

Table 2.1: The molecular constants for calcium monofluoride for the electronic, vibrational and rotational energy terms up to second order for the ground, the first and second excited state [27].

Parameter	$X^2\Sigma^+$	$A^2\Pi_{1/2}$	$B^2\Sigma^+$
$T_{\mathrm{el}}\,(1/\mathrm{cm})$	0	16525.613	18841.309
$\omega_{\mathrm{e}}\,(1/\mathrm{cm})$	588.644	594.513	572.405
$\omega_{\mathrm{e}}\chi_{\mathrm{e}}\,(1/\mathrm{cm})$	2.91194	3.031	3.143
$B\,(1/\mathrm{cm})$	0.34370924	0.348781	0.342604
$D\,(1/\mathrm{cm})$	$4.688 \cdot 10^{-7}$	$4.808 \cdot 10^{-7}$	$4.829 \cdot 10^{-7}$
$A\,(1/\mathrm{cm})$	-	71.429	-

In this equation ω_{e} is the harmonic approximation of the frequency of the potential, $\omega_{\mathrm{e}}\chi_{\mathrm{e}}$ the anharmonicity constant and ν the vibrational quantum number ($\nu = 0, 1, 2, ...$).

Equations (2.1.4) and (2.1.7) approximate the rotational and vibrational energy terms. Higher orders of these energy terms can be calculated by solving the time-independent Schrödinger equation of the molecule [17, 30].

The electronic Hamiltonian, the rotational Hamiltonian, the vibrational Hamiltonian and the spin-orbit interaction are the largest contributors to the effective Hamiltonian. The hyperfine structure Hamiltonian only gives a small contribution to the total energy of each state, but it is crucial for a magneto-optical trap, as described in subsection 2.2.1. Other contributions are for example Λ-doubling and the centrifugal distortion term [31, 32], and are neglected here. This leads to the total energy approximately being

$$E_{\mathrm{tot}} \approx E_{\mathrm{el}} + E_{\mathrm{vib}} + E_{\mathrm{rot}} + E_{\mathrm{so}} + E_{\mathrm{HFS}}. \tag{2.1.8}$$

With the first four energy terms, and neglecting E_{HFS}, the transition frequencies can be calculated to an accuracy over 99.9%. The electronic energy levels are given by $E_{\mathrm{el}} = hc \cdot T_{\mathrm{el}}$ with T_{el} being the electronic constant of a state. Furthermore the spin-orbit energy is approximately $E_{\mathrm{so}} \approx A\Lambda\Sigma$. Here A is the fine-structure coupling constant and Λ and Σ projections of the electric orbital momenta and spin angular momenta projected onto the internuclear axis [31]. Finally, E_{HFS} is the hyperfine structure.

Table 2.1 lists the molecular constants of CaF. Inserting these into the effective Hamiltonian results in the molecular energy structure which is shown in Figure 2.3.

Transitions between states have to obey certain selection rules, which are listed in Table 2.2. An important consequence of these is that it is possible to identify closed optical cycles. In laser cooling of CaF the $X^2\Sigma^+(N = 1)$ state is used as the ground state, because due to the selection rules, the $X^2\Sigma^+(\nu = 0) \longrightarrow B^2\Sigma^+(\nu = 0)$ transition is rotationally closed [10].

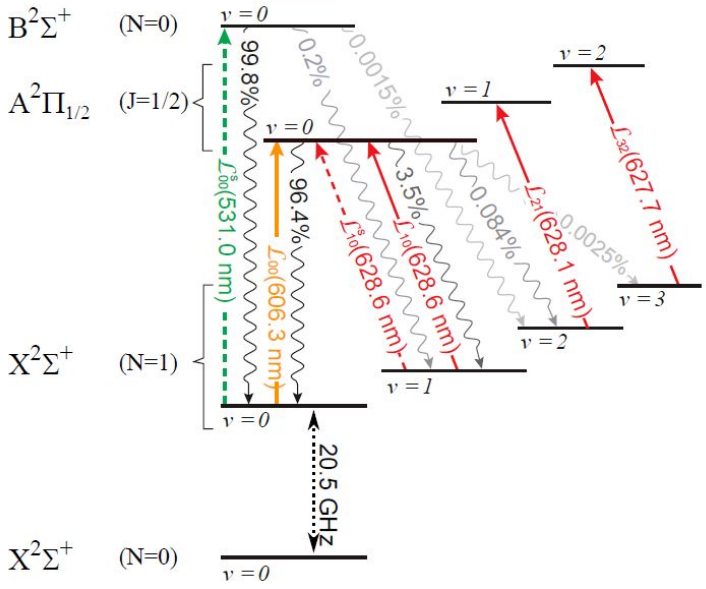

Figure 2.3: Energy level scheme of CaF. Depicted are the ground state and the first and second excited states as well as relevant vibrational level. The transition frequencies and the Frank-Condon factors are also shown. Figure taken from [29].

Table 2.2: Selection rules governing electric dipole transitions [29].

Parity	$\Delta P = \pm 1$
Vibration	no rule
Rotation	$\Delta N = 0, \pm 1,\ N = 0 \not\leftrightarrow N' = 0,\ \Delta m_F = 0, \pm 1$

The Frank-Condon factors are the transition probabilities of the spontaneous decays between two vibrational states of the molecule. The Franck-Condon factor of a decay is calculated via the overlap of the wave functions of the two energy states. CaF has good Franck-Condon factors, that lead to the molecule highly likely decaying into the same states, as shown in Figure 2.3. Hence, only a few additional lasers are needed in order to reintroduce the molecules back into the cooling cycle. The transition wavelengths and their function in the cooling process are listed in Table 2.3.

In the following, abbreviations for the transitions are used. The ground state $X^2\Sigma^+$ as well as the electronically excited states $A^2\Pi_{1/2}$ and $B^2\Sigma^+$ are shortened to X, A and B respectively. The vibrational quantum number of the state is added in brackets. Thus the transitions are X(0)-B(0), X(0)-A(0), X(1)-A(0), X(2)-A(1) and X(3)-A(2).

Moreover, the energy levels depicted in Figure 2.3 have a substructure due to hyperfine splitting. Figure 2.4 shows the hyperfine structure of the X, A and B states. Note that the

Table 2.3: Transitions, approximated wavelengths and required powers [29, 33].

Laser beam	Transition	Wavelength λ (nm)	Power P (W)
Slowing laser	$X^2\Sigma^+(\nu = 0) \longrightarrow B^2\Sigma^+(\nu = 0)$	531.0	1 [34]
Cooler	$X^2\Sigma^+(\nu = 0) \longrightarrow A^2\Pi_{1/2}(\nu = 0)$	606.3	1
First repumper	$X^2\Sigma^+(\nu = 1) \longrightarrow A^2\Pi_{1/2}(\nu = 0)$	628.6	1
Second repumper	$X^2\Sigma^+(\nu = 2) \longrightarrow A^2\Pi_{1/2}(\nu = 1)$	628.1	0.1
Third repumper	$X^2\Sigma^+(\nu = 3) \longrightarrow A^2\Pi_{1/2}(\nu = 2)$	627.7	0.01

X and B state have a well resolved hyperfine splitting, while the A state does not. Only one vibrational state of each electronic state is shown, because the hyperfine structures of the other vibrational states are very similar within the electronic state. Eventually all hyperfine structure states have to be addressed so that no decay channels to hyperfine dark states exist.

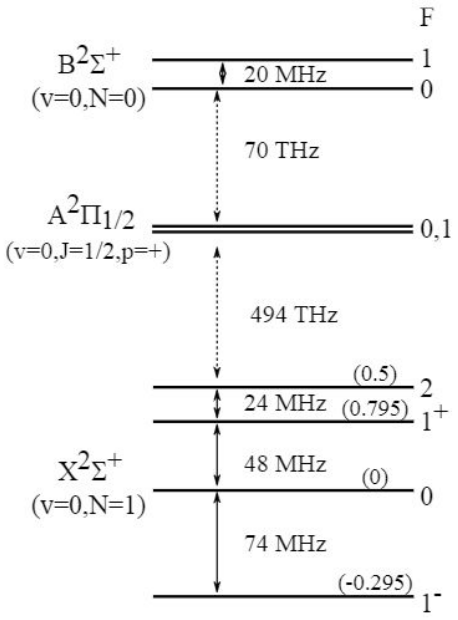

Figure 2.4: Hyperfine structure of the ground, first and second excited states. Figure taken from [29].

2.1.3 Laser cooling of calcium monofluoride

The X(0)-A(0) and the X(0)-B(0) transitions are almost closed transitions due to their highly diagonal Franck-Condon factors. Therefore they are good transitions for laser cooling of CaF.

The X(0)-B(0) transition is used as the molecular beam slower, due to its highly diagonal Franck-Condon factors. Therefore many scattering processes can occur before the molecule decays into a state which is not addressed by a laser. To slow a molecule from approximately 200 m/s to a velocity of around 10 m/s, the molecule has to scatter approximately 10^4 photons.

The X(0)-A(0) transition is used as the main cooling transition in the magneto-optical trap. The trapping force is largest by using this particular transition [35].

The repumper lasers with the transitions X(1)-A(0), X(2)-A(1) and X(3)-A(2) reintroduce molecules from higher vibrational states back into the cooling cycle. In this case, the effective scattering rate Γ_{eff} scales with $\Gamma_{\text{eff}} \propto \frac{N_{\text{e}}}{N_{\text{g}}+N_{\text{e}}}$, where N_{e} is the number of excited states and N_{g} the number of ground states [32].

The CaF molecules can also decay into dark states. These states can not be reintroduced into the cooling cycle, even if the correct transition frequency is present. Dark states can appear due to a static polarization of light or because of the transitions to the excited states are forbidden due to conservation of angular momentum. For example, assume a molecule in a ground state with $F = 1$ and an excited state with $F = 0$ situated in a π-polarized light field. The linear polarized light field addresses transitions with $\Delta m_F = 0$. So, the $m_F = 0$ level in the ground state is a bright state to this light field because it can be addressed by it. In contrast, the $m_F = \pm 1$ levels are dark states to this light field [10, 32]. Solutions to prevent the formation of dark states generally either switch the polarization of the light between orthogonal states or choose the polarization of the light that the dark state of this light field is a superposition of states. If a small magnetic field is applied, the dark state will destabilize and therefore evolve into a bright state [10]. In this experiment, we plan to address different levels of the hyperfine structure with different polarizations to prevent the formation of dark states for the X-A transitions [36].

2.2 Molecular traps

2.2.1 Magneto-optical trapping of calcium monofluoride

In the standard Doppler cooling described above, the molecules interact with a velocity dependent force. While this can cool the molecules, it will not trap them. The molecules can still diffuse out of the cooling region. An additional position-dependent force is created by adding a magnetic field gradient. Traps operating with such a scheme are called magneto-optical traps (MOT). Figure 2.5 shows a scheme of a MOT, depicting the magnetic field with the yellow and green arrows and the light beams together with their polarization.

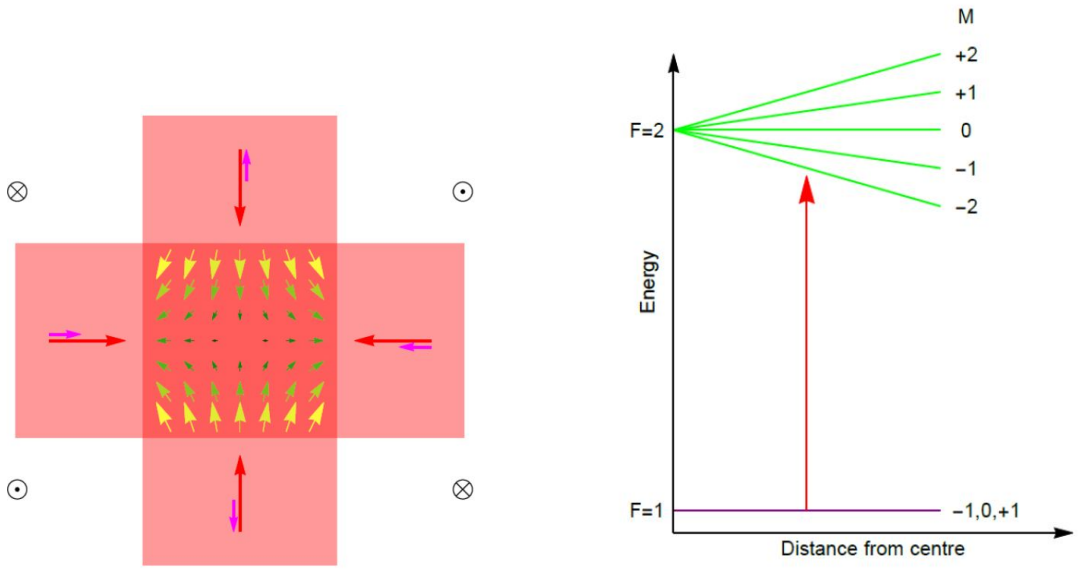

(a) (b)

Figure 2.5: (a) General principle of a magneto-optical trap. The yellow and green arrows indicate the direction and the strength of the magnetic field. The propagation directions of the light beams are the red arrows. The purple arrows depict the photon-spin and thus their polarization. (b) Energy level diagram for a ground state with $F = 1$ and no Zeeman shift and an excited state with $F' = 2$ and a significant Zeeman shift. The energy splitting of the excited state increases linearly with the distance from the trap center. Figures taken from [10].

For simplicity, we consider a MOT in 1D along the z-axis. Along this axis there is a linear magnetic field gradient. Molecules away from the center of the trap thus experience a larger Zeeman shift. Counter propagating laser beams are red-detuned and have different circular polarizations. Therefore the σ^+-beam will increase m_F by one, the σ^--beam will decrease m_F by one. States with different angular quantum number m_F have different energy levels due to the Zeeman splitting, as pictured in Figure 2.5b. This leads to one beam being closer to their transition resonance than the other, causing more photons to be scattered from one beam than the other. This leads to a net radiation pressure towards the center.

MOTs can be split into two types, type I and type II MOTs. A type I MOT addresses $F \rightarrow F + 1$ transitions. This makes these transitions easy to control, since only one laser is needed. Most atomic MOTs are of type I. Type II MOTs drive $F \rightarrow F$ or $F \rightarrow F - 1$ transitions. The excited state can decay into other states than the initial state. Thus more transitions need to be addressed to control the MOT [37]. For CaF a type II MOT is

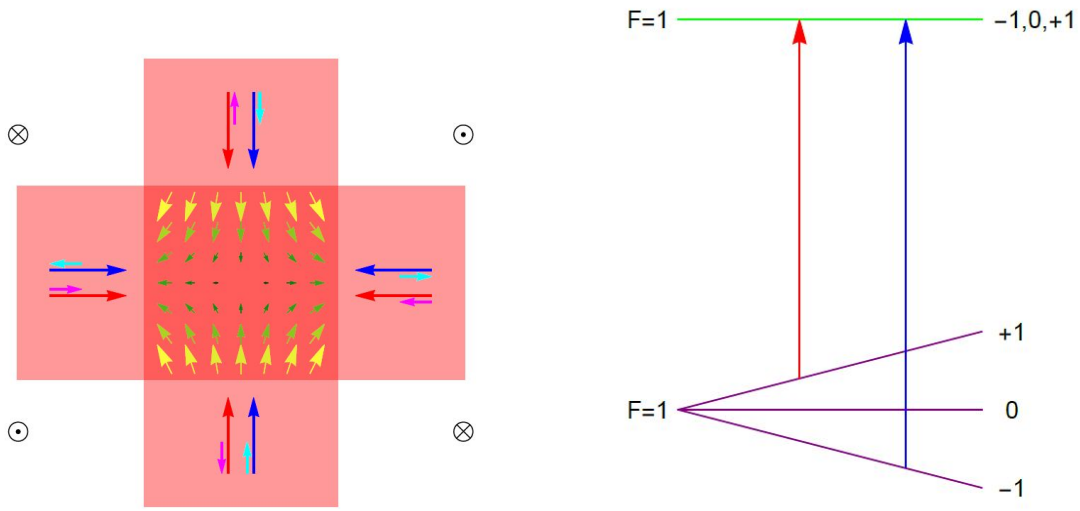

(a) (b)

Figure 2.6: Scheme of a dual frequency MOT and the transitions which the detuned beams address in the energy level scheme. (a) Two beams through the magnetic field gradient in each direction with opposite polarization. (b) The detuned lasers address the split levels and prevent the formation of dark states. Figures taken from [10].

required, because there are four hyperfine structure states with $F = 2, 1, 0, 1$ in the ground state and two hyperfine states with $F' = 1, 0$ in the first excited state [36].

Two common ways make a MOT with CaF. The first is the radio-frequency MOT, where polarization switching takes care of the dark states. Second, the dual frequency MOT, where a second blue-detuned beam is added to excite molecules from their previous dark states. The experiment which we are constructing will use a dual frequency MOT. In a dual frequency MOT there are two beams in each direction. One laser beam is red-detuned and the other blue-detuned. The two beams have opposite circular polarization. This setup prevents the formation of dark states, because the beams address the transitions with the largest and smallest m_F due to their detuning. Thus, all states can be addressed. Figure 2.6 shows a scheme of a dual frequency MOT.

Since blue-detuned Doppler forces cause heating, the blue-detuned beam is detuned further than the red-detuned beam. This ensures that cooling forces dominate, because then photons from the red-detuned beam are more likely to be scattered. Hence, trapping and cooling can be achieved with the dual frequency MOT.

The Doppler temperature that can be achieved in a MOT is not cold enough to reach the phase transition to a Bose-Einstein condensate. Therefore, this experiment will use sub-

Doppler cooling mechanisms. One of these is evaporative cooling, where the hottest particles in an ensemble are removed, so that the ensemble thermalizes at a lower temperature.

2.2.2 Optical dipole traps

Optical dipole traps can perform evaporative cooling. This method can lead to arbitrarily low temperatures, albeit at a significant particle number loss. In evaporative cooling the trapping potential is lowered, such that the most energetic molecules leave the trap. Thus, the average energy per remaining molecule is reduced, and after rethermalization via collisions the temperature of the ensemble is lower than before. This process can be repeated many times until a desired temperature is reached.

In the oscillator model, the interaction of the particle with light is modeled by an oscillator [11]. The dipole force arises due to the interaction of the induced dipole moment with the intensity gradient. Let us consider an electric field $\mathbf{E}$ which induces a dipole moment $\mathbf{p}$ in the particle. For an oscillating electric field with the frequency ω and $\hat{\mathbf{e}}$ the unit polarization vector we have

$$\mathbf{E}(\mathbf{r},t) = \hat{\mathbf{e}} \cdot E(\mathbf{r}) \cdot e^{-i\omega t} \quad \text{and} \tag{2.2.1}$$

$$\mathbf{p}(\mathbf{r},t) = \hat{\mathbf{e}} \cdot p(\mathbf{r}) \cdot e^{-i\omega t} \quad \text{with} \tag{2.2.2}$$

$$p = \alpha E, \tag{2.2.3}$$

with α being the complex polarizability of the atom or molecule. The interaction potential $U_{\text{dip}}(\mathbf{r})$ of the induced dipole moment with the electric field is given by

$$U_{\text{dip}}(\mathbf{r}) = -\frac{1}{2}\langle \mathbf{pE} \rangle = -\frac{1}{2\epsilon_0 c}\text{Re}(\alpha) I(\mathbf{r}). \tag{2.2.4}$$

Here $I(\mathbf{r})$ is the intensity of the light field, ϵ_0 the vacuum permittivity and c the speed of light. The gradient of the interaction potential is the dipole force. It is given by

$$\mathbf{F}_{\text{dip}}(\mathbf{r}) = -\nabla U_{\text{dip}}(\mathbf{r}) = \frac{1}{2\epsilon_0 c}\text{Re}(\alpha)\nabla I(\mathbf{r}). \tag{2.2.5}$$

For practical interest the dipole potential U_{dip} and the scattering rate Γ_{sc} are well approximated by

$$U_{\text{dip}}(\mathbf{r}) = \frac{3\pi c^2}{2\omega_0^3}\frac{\Gamma}{\Delta} I(\mathbf{r}) \tag{2.2.6}$$

and

$$\Gamma_{\text{sc}}(\mathbf{r}) = \frac{3\pi c^2}{2\hbar\omega_0^3}\left(\frac{\Gamma}{\Delta}\right)^2 I(\mathbf{r}). \tag{2.2.7}$$

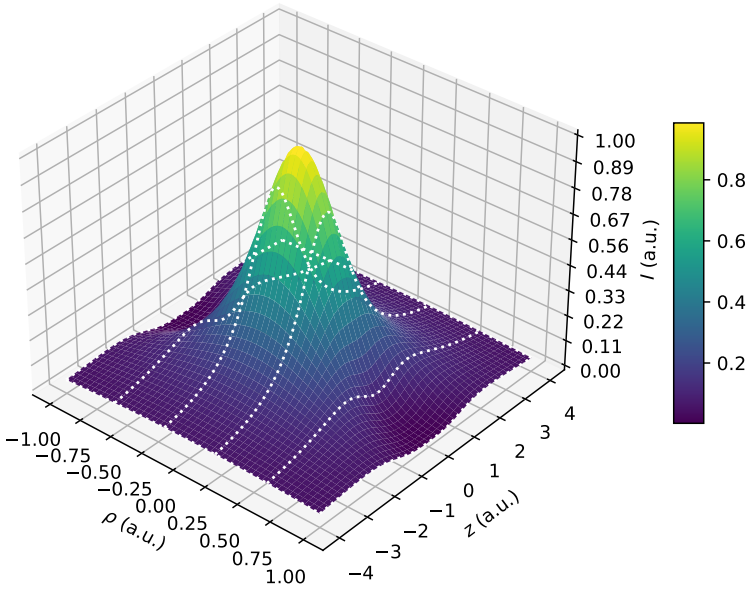

Figure 2.7: Intensity profile of a Gaussian beam. The intensity maximum is located in the center of the beam. In accordance with equation (2.2.6), particles will be attracted towards or repelled from the center of the beam depending on the sign of the detuning Δ.

Here ω_0 is the transition frequency of the of the particle, Γ the linewidth of the excited state and Δ the detuning of the laser light. The scattering rate describes the number of absorption and spontaneous reemisson processes of the oscillator.

The dipole trap laser beam can be modeled as a Gaussian beam. Figure 2.7 shows an intensity profile of such a beam. The global maximum of the intensity is positioned at the waist of the beam, which is also the trap center. The dipole force is the gradient of the intensity, and thus points into or away from the direction of the steepest increase.

The interaction potential is inversely proportional to the detuning Δ of the beam. Therefore, a red detuned beam with $\Delta < 0$ leads to an attractive force towards the trap's center. A blue detuned beam with $\Delta > 0$ leads to an repulsive force. It is favorable to have a large trap depth and low scattering rates. The dipole potential scales with $U_{\mathrm{dip}}(\mathbf{r}) \propto \frac{I}{\Delta}$, while the scattering rate scales with $\Gamma_{\mathrm{sc}} \propto \frac{I}{\Delta^2}$. This is the reason why high intensities and large detunings are used.

Optical dipole traps can be traps of many different shapes, including cigar-shaped traps, crossed dipole traps or blue-detuned light sheets. The latter are used to create steep potential walls [11]. Furthermore, since the trap depth is proportional to the intensity of the light field, dipole traps can be made very deep by employing high-power lasers. A

strong confinement is helpful because it leads to a higher density and thus a higher collision rate, which in turn increases the efficiency of the evaporative cooling process.

2.3 Optics & lasers

2.3.1 Gaussian beam optics

A laser beam is well approximated by the Gaussian beam. The theoretical description outlined here is based on B. Saleh and M. Teich's book "Fundamentals of Photonics" [38]. The Gaussian beam is a solution to the paraxial Helmholtz equation. It is given by

$$\nabla_T^2 A(\mathbf{r}) - 2ik\frac{\partial A(\mathbf{r})}{\partial z} = 0, \tag{2.3.1}$$

where $A(\mathbf{r})$ is the complex envelope of the complex amplitude, $k = \frac{2\pi}{\lambda}$ is the wavenumber and $\nabla_T^2 = \frac{\partial^2}{\partial x^2} + \frac{\partial^2}{\partial y^2}$ is the transverse part of the Laplacian operator. The complex envelope of the Gaussian beam is given by

$$A(\mathbf{r}) = \frac{A_1}{q(z)} \exp\left(-ik\frac{\rho}{2q(z)}\right) \quad \text{with} \tag{2.3.2}$$

$$q(z) = z + iz_0, \tag{2.3.3}$$

where A_1 is the amplitude, $\rho^2 = x^2 + y^2$ is the squared radial coordinate and z_0 is the Rayleigh range. Inserting this equation into $U(\mathbf{r}) = A(\mathbf{r})\exp(-ikz)$ leads to the complex amplitude of the Gaussian beam. It is given by

$$U(\mathbf{r}) = A_0\frac{w_0}{w(z)} \exp\left(-\frac{\rho^2}{w^2(z)}\right) \exp\left(-ikz - ik\frac{\rho^2}{2R(z)} + i\xi(z)\right). \tag{2.3.4}$$

The beam width is $w(z)$, the wavefront radius curvature is $R(z)$, the Gouy phase is $\xi(z)$ and $A_0 = \frac{A_1}{iz_0}$. These are given by

$$w(z) = w_0\left[1 + \left(\frac{z}{z_0}\right)^2\right]^{\frac{1}{2}}, \tag{2.3.5}$$

$$R(z) = z\left[1 + \left(\frac{z_0}{z}\right)^2\right], \tag{2.3.6}$$

$$\xi(z) = \arctan\left(\frac{z}{z_0}\right) \quad \text{and} \tag{2.3.7}$$

$$w_0 = \left(\frac{\lambda z_0}{\pi}\right)^{\frac{1}{2}}. \tag{2.3.8}$$

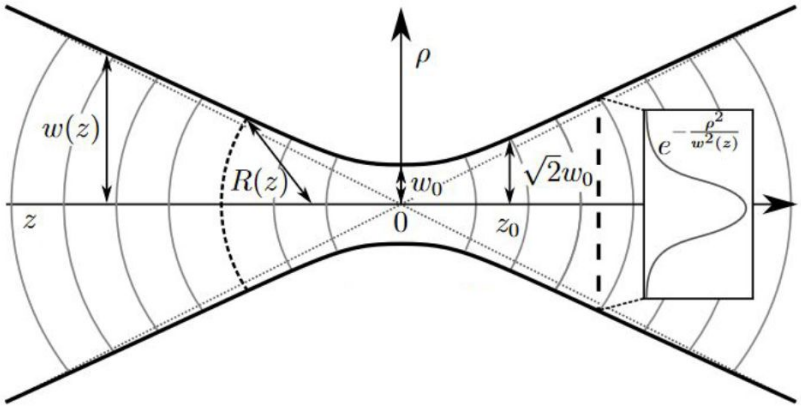

Figure 2.8: Profile of a Gaussian beam. The beam waist is at $z = 0$. The beam intensity follows a Gaussian curve. Figure taken and modified from [39].

The profile of a Gaussian beam is depicted in Figure 2.8. Due to the rotational symmetry around the propagation axis, a 2D plot is sufficient.

The intensity profile of the Gaussian beam is given by

$$I(\mathbf{r}) = |E(\mathbf{r})|^2 = I_0 \left(\frac{w_0}{w(z)} \right)^2 \cdot \exp\left(-\frac{2\rho^2}{w^2(z)} \right) \tag{2.3.9}$$

and depicted in Figure 2.7.

Propagation through a thin lens If a Gaussian beam propagates through a thin lens the radius of curvature changes. It holds

$$\frac{1}{R'} = \frac{1}{R} - \frac{1}{f}\,. \tag{2.3.10}$$

This condition can also be expressed through the old and new beam waist. This is given by

$$w_0' = \frac{w_0}{\sqrt{1 + \left(\frac{z_0}{f}\right)^2}}\,. \tag{2.3.11}$$

Here, f is the focal length of the lens. The propagation is shown in Figure 2.9.

2.3.2 Diode lasers

Principle The principle of a laser is stimulated emission of photons in an active medium. A resonator amplifies the light emitted by the active medium and provides feedback. An

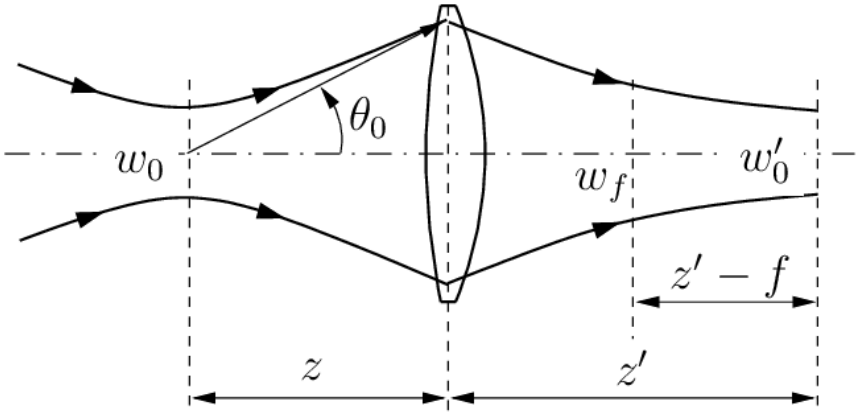

Figure 2.9: Propagation of the Gaussian beam through a thin lens. The beam waist w_0' and the position of the beam waist z' change. Figure taken from [40].

external energy source excites the active medium, so that population inversion is achieved. The active medium can not be a two level system, because the Einstein coefficients for excitation and disexcitation would be the same. It has to be a three or higher level system, so that population inversion can be achieved. Spontaneous decay in the active medium emits a photon and this will induce stimulated emission of further photons. This is a chain reaction and triggers a photon avalanche. The laser resonator selects a specific mode and amplifies a specific wavelength.

Working principle The active medium in a diode laser is a two-layer doped semiconductor. One layer is a n-type, the other p-type. The ground state of the electron in its level system is in the valence band, the excited state in the conduction band. Population inversion is achieved by electrical pumping. By applying a current in the forward direction of the diode electron recombination in the pn-junction is achieved and a photon with the energy of the energy gap is emitted. This process is depicted in Figure 2.10a.

The active medium has a highly reflective back and a partially reflective front. This forms a resonator which amplifies the light, by reflecting photons back into the active medium which causes stimulated emission. Figure 2.10b shows a scheme of a laser diode.

Littrow configuration The Littrow configuration is a construction type of a diode laser with an external cavity. The main function of the external cavity is selecting a laser mode. One of the mirrors is a blaze grating, where its profile is shown in Figure 2.11.

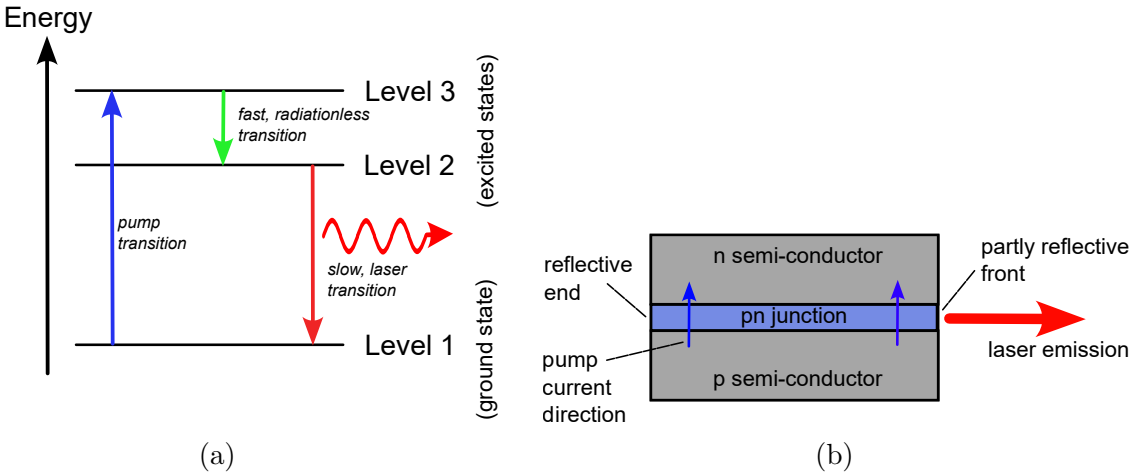

Figure 2.10: (a) Three-level energy scheme that leads to population inversion. The pump transition is driven by an electric current. A photon is emitted when decaying from level 2 to level 1. (b) Simple laser diode scheme. Electron recombination takes place in the junction.

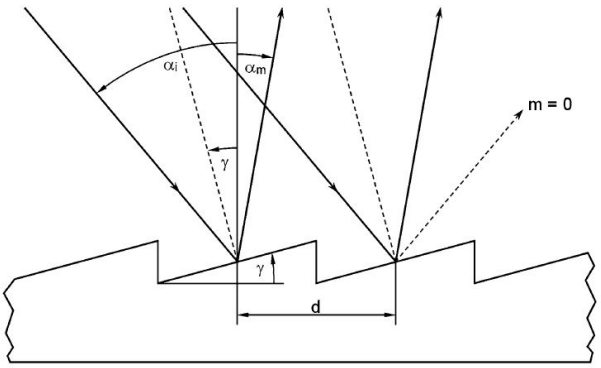

Figure 2.11: Profile of a blaze grating. This profile is a ruled grating, with d being the line grating. Figure taken from [41].

The Littrow configuration is indicated by equal incidence angle α_i and emergent angle α_m. It holds

$$\alpha_i = \alpha_m = \alpha_L. \tag{2.3.12}$$

In the Littrow configuration the condition for constructive interference is given by

$$2d \cdot \sin(\alpha_L) = n \cdot \lambda. \tag{2.3.13}$$

Here d is the line spacing, λ the wavelength and n an integer [42]. The optical power in this configuration is minimized for the zeroth reflection order and maximized for the first. The first reflection order overlaps exactly with the incoming beam and thus provides feedback. The reflected light beam under the emergent angle is outcoupled. Best efficiencies are achieved if the blaze angle γ is equal to the Littrow angle α_L.

In our diode lasers we use ruled gratings. The surface of such a grating, shown schematically in Figure 2.11, has a serrodyne shape. Holographic gratings, as used in the second repumper, have a wave-like profile. An advantage of the Littrow configuration is that the wavelength can be modified by changing the grating angle.

Properties Diode lasers have a small linewidth in the MHz range. This is well-suited for addressing cooling transitions, which typically have similar linewidths. Moreover, diode lasers can emit up to a few 100 mW of power. The diode lasers used in this thesis emit up to 130 mW ($\lambda = 1212$ nm) and 110 mW ($\lambda = 1256$ nm).

Laser diodes are available for the wavelengths in the ranges between 375 nm and 515 nm, as well as from 630 nm to 2000 nm. Unfortunately the X(0)-A(0), X(1)-A(0) and X(0)-B(0) at 606.3 nm, 628.6 nm and 531.0 nm respectively fall within the range where no laser diodes are available. However, laser radiation at these wavelengths can be achieved by using second-harmonic generation (SHG), which is a nonlinear process in which two photons form a new photon with twice the frequency. With this, it is possible to first use a diode laser at twice the targeted wavelength where sufficient power is readily available. The two diode lasers used in this thesis are diode lasers with wavelengths 1212.6 nm and 1257.2 nm, which then are frequency doubled to generate the desired wavelengths at 606.3 nm and 628.6 nm.

2.3.3 Second harmonic generation

The theory presented in this section is based on W. Demtröder's book "Experimentalphysik 2: Elektrizität und Optik" (2012) [43]. In nonlinear optics the polarization density $\mathbf{P}$ of a medium is given by

$$\mathbf{P}(t) = \epsilon_0 \cdot (\chi^{(1)}\mathbf{E}(t) + \chi^{(2)}\mathbf{E}^2(t) + \chi^{(3)}\mathbf{E}^3(t) + ...)\,, \tag{2.3.14}$$

where $\chi^{(n)}$ is the susceptibility of n-th order. The response of the medium of an external electric field $\mathbf{E}(t)$ is given by $\mathbf{P}(t)$. If a monochromatic wave of the form

$$\mathbf{E} = \mathbf{E_0} \cdot \cos(\omega t - kz) \tag{2.3.15}$$

with the frequency ω, the time t, the wavenumber k and the propagation distance z propagates through the medium, higher harmonics will appear due to the higher order contributions of $\mathbf{E}$.

Inserting equation (2.3.15) into equation (2.3.14) as well as assuming that terms higher than quadratic are negligible, that $z = 0$ and that $\mathbf{E_0} = (E_{0x}, 0, 0)$ leads to

$$P_x = \epsilon_0 \cdot (\chi^{(1)} E_{0x} \cos(\omega t) + \chi^{(2)} E_{0x}^2 \cos^2(\omega t)) \tag{2.3.16}$$

$$= \epsilon_0 \cdot (\chi^{(1)} E_{0x} \cos(\omega t) + \frac{1}{2}\chi^{(2)} E_{0x}^2 (1 + \cos(2\omega t))) \,. \tag{2.3.17}$$

The last term in equation (2.3.17) oscillates with twice the frequency of the input field, thus second-harmonic generation (SHG) is achieved. Two waves, one with the frequency ω and one with 2ω, are emitted at every point in space in the medium. For constructive interference of microscopic waves of the dipoles at every point in space to macroscopic waves they have to be in phase at every point. Therefore, the phase velocities of incoming and frequency doubled wave have to be equal.

Birefringence of an anisotropic material is useful for phase matching. In such materials, a certain propagation direction of the beam with a specific angle Θ_p to the optical axis leads to the same refractive index n for the two waves with the frequencies ω and 2ω. As $n_\mathrm{a}(2\omega) = n_\mathrm{o}(\omega)$, the phase velocities are equal: $v_\mathrm{ph}(2\omega) = v_\mathrm{ph}(\omega)$. However, there is also a downside of this phase matching method. The phase matching condition is only satisfied if the incoming wave with a specific direction and angle to the optical axis fit to the wavelength. Optimization to a certain wavelength must be done through rotation of the crystal axis. Furthermore the efficiency of the SHG is dependent on the polarization of the incoming wave. Another method is quasi phase matching. Here a ferroelectric crystal consisting of many layers with periodically alternating spacial polarity is used. The layers have a refractive index of $\pm\Delta n = n(2\omega) - n(\omega)$. The phase difference created in the first layer will be compensated by the second layer and so on. Overall the output power of the frequency doubled wave will not be as high as using proper phase matching after the same crystal length but quasi phase matching can be used for a wide range of wavelengths [43]. The performance of the two methods is pictured in Figure 2.12. They are also compared to a crystal with slight mismatch. l_c is the critical phase matching length. After this length the phase difference between initial and frequency-doubled wave is π.

2.3.4 Raman fiber amplifier

Our experiment needs powers in the range of $1 - 2\,\mathrm{W}$. Since the process of SHG requires high input powers, we use amplifiers to increase the power of the diode lasers.

To reach the high laser powers required for this experiment we use Raman fiber amplifiers. These amplifiers are based on Raman gain, which is a result of stimulated Raman scattering. In Raman scattering, photons scatter inelasticly by matter, which can change the energy of the photon during the scattering process. The magnitude of the gain depends on the frequency difference ($\Delta\nu$) between the pump and signal wave. The signal wave is Stokes-shifted via Raman scattering, meaning that the photons lose energy through the scattering

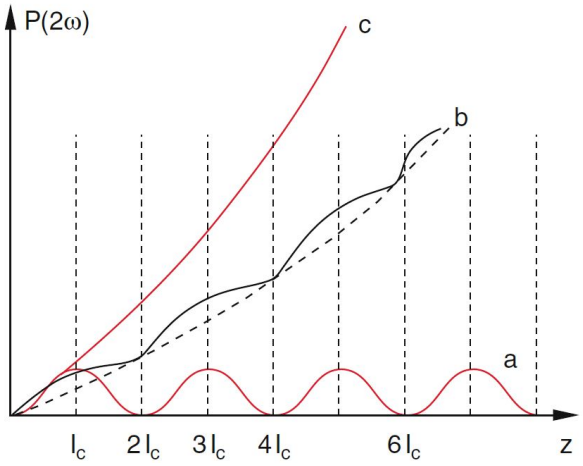

Figure 2.12: Output power of the frequency-doubled wave $P(2\omega)$ for different methods. (a) crystal with a slight mismatch. (b) quasi phase matching with same slight mismatch. (c) crystal with ideal phase matching. Figure taken from [43].

process. The interaction of these is given by the coupled differential equations

$$\frac{\partial I_\mathrm{s}}{\partial z} = g_\mathrm{R}(\Delta\nu) I_\mathrm{p} I_\mathrm{s} \quad \text{and} \tag{2.3.18}$$

$$\frac{\partial I_\mathrm{p}}{\partial z} = -\frac{\nu_\mathrm{p}}{\nu_\mathrm{s}} g_\mathrm{R}(\Delta\nu) I_\mathrm{p} I_\mathrm{s}, \tag{2.3.19}$$

where I and ν are the intensity and frequency of either the pump (p) or signal (s) wave, z the distance along the z-axis and $g_\mathrm{R}(\Delta\nu)$ the Raman gain coefficient. So, if the Raman gain is larger than propagation losses, then the signal is amplified [44].

Typically Raman-scattering and thus Raman amplifying is done with Yb-doped fibers. The light of the diode lasers is inputted into these fibers, which are pumped by a current. The output of these is amplified input light.

2.3.5 Fabry-Perot interferometers

Fabry-Perot interferometers act as frequency filters and thus are an essential part for frequency locking. The goal of frequency locking is frequency stabilization of our diode lasers, because a free-running diode laser will experience a frequency drift due to fluctuations of external factors (for example temperature and pressure of the environment). In this experiment, the slave lasers will be locked to a master laser via their relative position on the cavity, which corresponds to their frequency. Cavity fluctuations affect all lasers equally, therefore only the frequency drifts of the diode lasers will be visible on the cavity. In sum, the stability of the master laser is transferred to the slave laser(s) via the cavity [45].

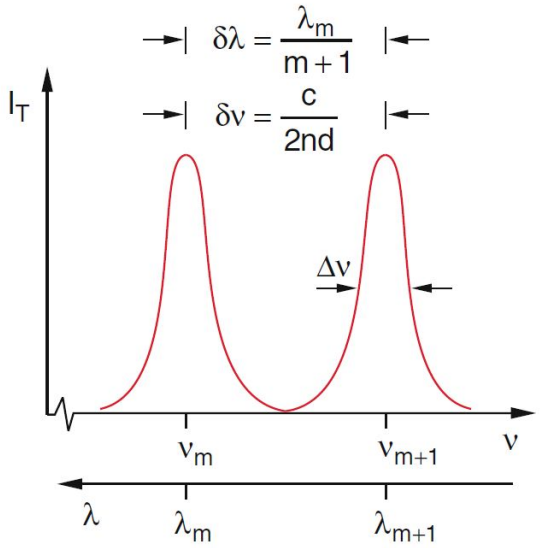

Figure 2.13: Intensity of the light beam in the resonator as a function of the frequency of the light in a Fabry-Perot interferometer. The free spectral range $\delta\nu$ and the full width at half maximum $\Delta\nu$ are sketched. Figure taken from [43].

Einius Pultinevicius[1] is currently working on a scanning transfer cavity lock, which will be implemented in this experimental setup.

Theory Fabry-Perot interferometers consist of two mirrors forming a resonator. The mirrors are highly reflective on one side and highly transparent on the other. The stability condition

$$0 \leq \left(1 - \frac{L}{\mathcal{R}_1}\right)\left(1 - \frac{L}{\mathcal{R}_2}\right) \leq 1, \tag{2.3.20}$$

where L is the distance between the two mirrors and $\mathcal{R}_1$ and $\mathcal{R}_2$ their curvatures [38] has to be satisfied by the mirrors in order to from a resonator.

The theoretical description of Fabry-Perot interferometers in this section is based on W. Demtröder's book "Experimentalphysik 2: Elektrizität und Optik" [43]. Figure 2.13 shows the intensity of the light beam transmitted through the resonator as a function of the frequency of the light beam.

The condition for constructive interference is given by

$$\lambda_m = \frac{2nd}{m}. \tag{2.3.21}$$

[1]Current Master student at University of Stuttgart

Here λ_m is the wavelength of the incident light, n the refractive index of the medium inside the interferometer, d the distance between the two mirrors and m an integer. The free spectral range expresses the period of the transmission curve for a specific wavelength λ or frequency ν. It is given by

$$\delta\lambda = \lambda_m - \lambda_{m+1} = \frac{\lambda_m}{m+1} \quad \Leftrightarrow \tag{2.3.22}$$

$$\delta\nu = \nu_{m+1} - \nu_m = \frac{c}{2nd}. \tag{2.3.23}$$

If the reflectivity of both mirrors are equal ($\mathsf{R}_1 = \mathsf{R}_2 = \mathsf{R}$), the full width at half maximum is given by

$$\Delta\nu = \frac{c}{2nd}\frac{1-\mathsf{R}}{\pi\sqrt{\mathsf{R}}}. \tag{2.3.24}$$

The free spectral range and the full width at half maximum are also depicted in Figure 2.13. The finesse F is a measure for the number of cycles before the light is transmitted out of the interferometer. It is defined as the ratio of free spectral range and full width at half maximum.

$$F = \frac{\delta\nu}{\Delta\nu} = \frac{\pi\sqrt{\mathsf{R}}}{1-\mathsf{R}} \tag{2.3.25}$$

The higher the finesse, the narrower the individual peaks will be. The transmitted intensity is given by

$$I_\mathrm{T}(\nu) = I_0\left[1 + \left(\frac{2F}{\pi}\right)^2 \sin\left(\frac{\pi\nu}{\delta\nu}\right)\right]^{-1}. \tag{2.3.26}$$

A scan over different resonance frequencies is performed by tuning the resonator length. Therefore a piezo is used because the length of the cavity can be tuned and its length increase is proportional to the applied voltage.

Mode matching The Gaussian beam in the resonator has to be mode matched so that the curvature of the beam matches the curvature of the mirrors $\mathcal{R}_{1/2}$, so

$$\mathcal{R}_1 = z_1 + \frac{z_0^2}{z_1} \quad \text{and} \tag{2.3.27}$$

$$\mathcal{R}_2 = z_2 + \frac{z_0^2}{z_2} \quad \text{with} \quad z_2 = z_1 + L, \tag{2.3.28}$$

where L is the length of the cavity. In the case of a plano-concave cavity one mirror is a plane mirror and the other concave [46]. Hence $\mathcal{R}_1 = \infty$ at $z_1 = 0$ and $\mathcal{R}_2$ is $\mathcal{R}_2(L) = L + \frac{z_0^2}{L}$

at $z_2 = L$. The curvature has to be modified by a lens in order to fulfill the condition. This leads to a condition for the waist w' after the lens being

$$w' = \sqrt{\frac{\lambda}{\pi}\sqrt{L\mathcal{R}_2 - L^2}}. \tag{2.3.29}$$

The focal length of the lens as well as its position can be derived by the equations in subsection 2.3.1. The lens will be positioned one focal length away from the resonator, so that the position of w' is at the position of the first mirror.

3 Experimental apparatus & characterization

In the first two sections of this chapter two lasers for the magneto-optical trap setup are characterized. Both lasers consist of a seed laser as well as a frequency-doubling stage. In section 3.1 the cooler is characterized.

Molecules that decay into other states are repumped back into the main cooling transition by repumping lasers. In section 3.2 the first repumper is characterized. This laser will compensate the most common decay into the first vibrationally excited state. Its setup is analogous to the cooler.

The setup of the second repumper is described in section 3.3. This laser is used to repump molecules from the second vibrationally excited state, so that the molecules can scatter approximately $4 \cdot 10^4$ photons before decaying out of the cycle.

Frequency locking of the cooler and first repumper is shown in section 3.4.

Finally, the dipole trap laser is characterized in section 3.5. Its power stability is measured and a setup for stabilization of short term power fluctuations is proposed. Furthermore, the radial and axial trap frequencies for a single beam dipole trap trapping calcium monofluoride are calculated.

3.1 Cooler

3.1.1 Setup of the cooler

Our experiment requires laser powers up to 2 W at a wavelength of 606.3 nm. This power is used for the cooler and for the transversal cooling of the molecular beam coming from the buffer gas cell. This beam is created by amplifying and frequency-doubling the light of a commercial diode laser[1], which serves as a seed laser, at 1212 nm with a visible Raman fiber amplifier (VRFA)[2].

The seed laser is constructed in Littrow configuration and the beam is directly fiber coupled via a fiber dock. The wavelength can be manually adjusted by adjusting the grating angle. This is done by turning the screw at the side of the housing, as pictured in Figure 3.1. The fine tuning of the grating angle is done by a built in piezo-electric element.

[1] *TOPTICA Photonics DL pro*
[2] *MPB Communications VRFA-P-2000-606-SF*

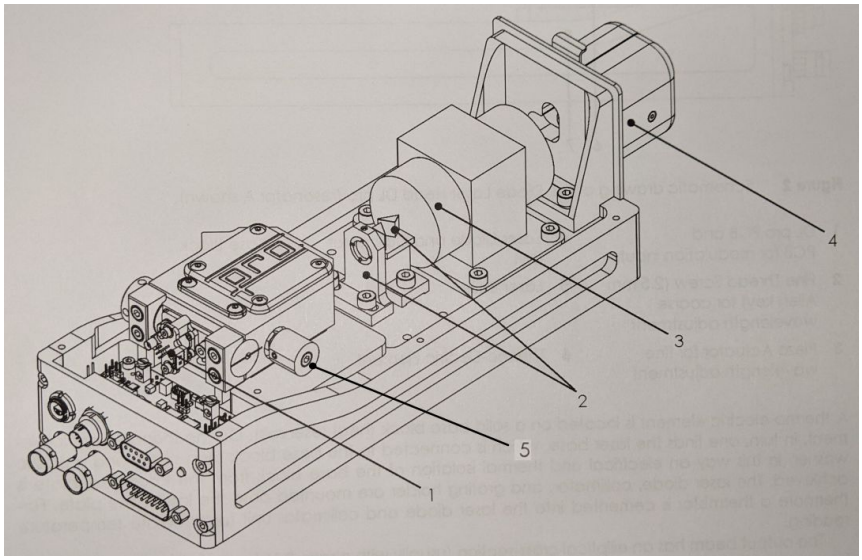

Figure 3.1: Schematic drawing of the diode laser with additional components. The components are: (1) Bias-T PCB (2) Beam shaping (3) Optical isolator (4) Fiber dock (5) Screw for rough adjustment of grating. Figure taken from [47].

The only other screws accessible are from the fiber dock. Inside are five screws for adjusting the x and y alignment of the whole fiber dock and the x, y and z alignment of the lens. Moreover, a port for adjusting the diode current is built in into the diode laser. This is used for frequency locking (see section 3.4).

The diode laser controller[3] controls the diode current and the temperature of the laser diode. Furthermore it controls also the voltage of the piezo-electric element for fine tuning of the grating angle.

Figure 3.2 shows a scheme of the setup of the VRFA. Its three components are an ytterbium fiber laser functioning as a pump laser, a visible Raman amplifier and the second harmonic generation (SHG) outcoupler. The VRFA is connected to the SHG outcoupler via the RFA output fiber. The ytterbium fiber laser component is also connected to a computer via USB. On the computer the graphical user interface is used for controlling and monitoring the SHG crystals temperature and the amplifier current. Moreover, the GUI displays the input and output powers of the amplifier and the SBS signal, which is a backwards propagating signal caused by stimulated Brillouin scattering [48]. First the beam coming from the seed laser is amplified by the Raman fiber amplifier. Second, in the SHG outcoupler the signal is frequency-doubled and then emitted. Not all light emitted will have a doubled frequency. Some light will remain with the initial frequency, as pointed out in equation (2.3.17). This light is filtered out and dumped in the outcoupler. Hence

[3] *TOPTICA Photonics DLC pro*

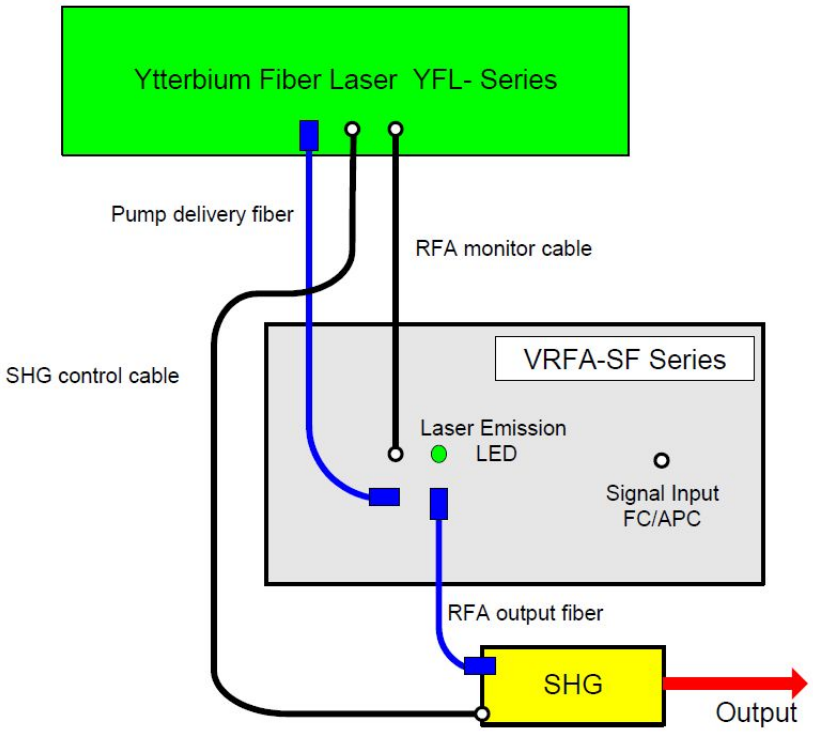

Figure 3.2: Scheme of the VRFA setup. The ytterbium fiber laser serves as a pump laser. This light will interact with the input signal from the seed laser in the visible Raman fiber amplifier. This leads to amplification of the input signal. In the SHG outcoupler the signal is frequency-doubled. The output is laser light with 606 nm in the case of the cooler and 628 nm in the case of the first repumper. Figure taken from [48].

the outputted light is only the frequency-doubled light.

The seed laser is connected to the amplifier via a fiber[4]. Since the incoupler of the amplifier is a simple fiber mount, fibers with the correct mode field diameter have to be used to connect the seed laser to the amplifier. The correct mode field diameter is in the range of 6 μm. The VRFA laser is operated via the GUI.

3.1.2 Seed laser characterization

The seed laser operates in the wavelength range between 1150.0 nm and 1249.4 nm [49]. Before any characterization measurements were performed the laser was tuned to 1212.6 nm (247.23 THz) manually by adjusting the grating. It is important that the seed laser emits

[4] *Thorlabs P3-980A-FC-2*

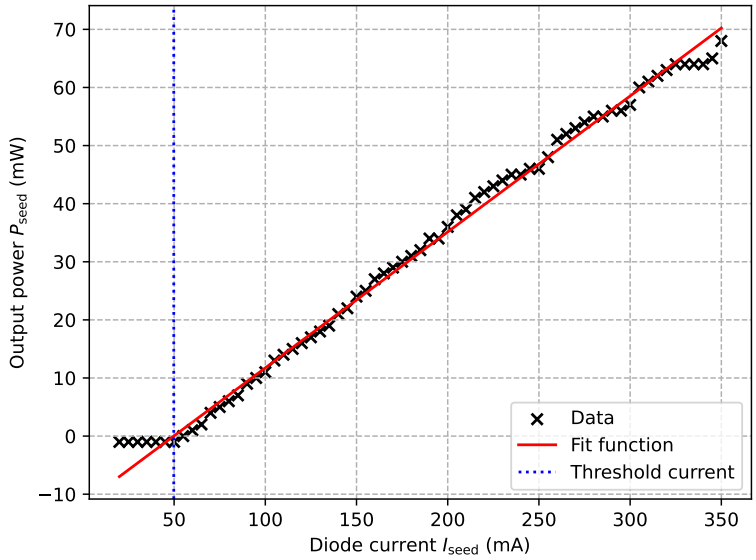

Figure 3.3: Measured output power of the 1212 nm seed laser of the cooler as a function of its diode current. The lasing threshold is at 49.8 mA and the slope efficiency is 0.234 mW/mA.

twice the frequency of the X(0)-A(0) transition. Furthermore the fiber coupling was optimized, so that maximum power would propagate through the fiber. The maximum power output, according to the data sheet of the laser, is $P_{\text{max,data sheet}} = 135.4\,\text{mW}$ at the maximum current $I_{\text{max,data sheet}} = 397\,\text{mA}$. Figure 3.3 shows the measured power P_{seed} emitted by the seed laser[5] as a function of its diode current I_{seed} at constant diode temperature $T_{\text{seed}} = 20\,°\text{C}$. The data points before the threshold current I_{th} are ignored for the fit. The fit function $P_{\text{seed}}(I_{\text{seed}})$ is given by

$$P_{\text{seed}}(I_{\text{seed}}) = m \cdot (I_{\text{seed}} - I_{\text{th}})\,. \tag{3.1.1}$$

The threshold is $I_{\text{th}} = 49.8\,\text{mA}$ and the slope efficiency is $m = 0.234\,\text{mW/mA}$. As soon as $I_{\text{seed}} > I_{\text{th}}$ the power rises almost linearly with rising current. The maximum power reached in this measurement is $P_{\text{max}} = 68.0\,\text{mW}$ at $I_{\text{max}} = 350\,\text{mA}$.

The data sheet lists the lasing threshold at $I_{\text{th,data sheet}} = 51.0\,\text{mA}$, the slope efficiency at $m_{\text{data sheet}} = 0.391\,\text{mW/mA}$ and the maximum power $P_{\text{max,data sheet}} = 135.4\,\text{mW}$ at the maximum diode current $I_{\text{max,data sheet}} = 397\,\text{mA}$ [49]. The observed lasing threshold is very close to the data sheet. However, the slope efficiency as well as the maximum power are both lower by a factor of approximately 0.6. The main reason for this is that the

[5]The power was measured with an *Thorlabs PM100A* with the power meter head being a *Thorlabs S314C*.

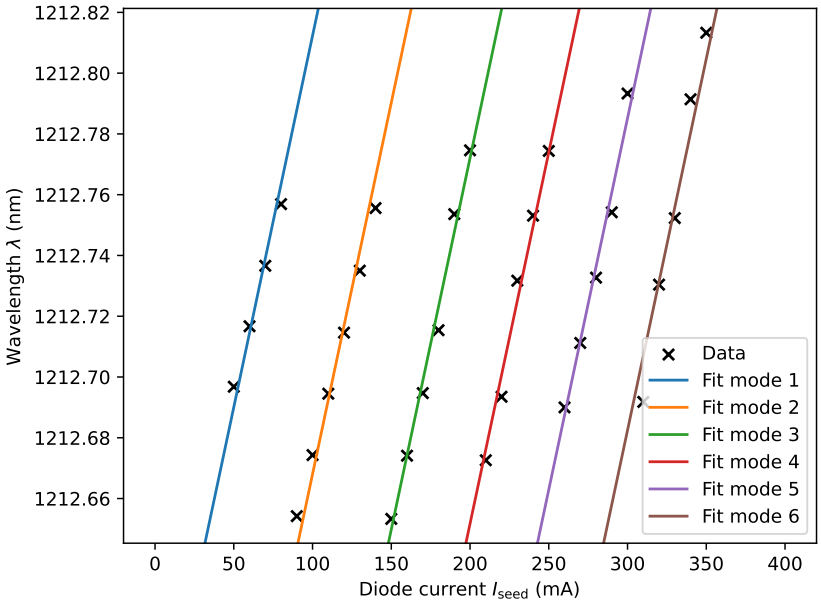

Figure 3.4: Measured wavelength λ as a function of diode current I_{seed} of the seed laser of the cooler. The wavelength of a mode rises linearly with the diode current. The average wavelength that can be tuned over before a mode jump occurs is $\Delta\lambda_I = 0.124\,\text{nm}$. The average gain of the modes is $0.002\,45\,\text{nm/mA}$.

measurement from the data sheet is in front of the optical isolator and fiber coupling [49], while the measurement here was performed behind these components. Nonetheless, the maximum emitted output power by the seed laser is fully sufficient for the amplifying and frequency-doubling stage since its maximum input power is limited to 50 mW.

The diode laser's wavelength depends mostly on the applied diode current and the temperature of the laser diode, once its grating angle is fixed. Figure 3.4 shows the wavelength as a function of the current at a constant temperature $T_{\text{seed}} = 20.0\,^{\circ}\text{C}$. In this plot six different modes are visible. The average gain of the modes is given by $m_{\lambda,I} = 0.002\,45\,\text{nm/mA}$, while the average spacing between two modes is given by $\Delta\lambda_I = 0.124\,\text{nm}$ ($\Delta f_I = 25.28\,\text{GHz}$). The large spacing between mode jumps is favorable, because the laser will stay on a mode during fine tuning.

Figure 3.5 shows the wavelength as a function of the diode temperature at constant diode current $I_{\text{seed}} = 200\,\text{mA}$. An increase in the diode temperature causes the output wavelength to change, because the resonance wavelength of the diode resonator changes. This can lead to mode jumps. Here, eight different modes with equal or more than three data points are visible. The average gain of the modes is given by $m_{\lambda,T} = 0.074\,\text{nm}/^{\circ}\text{C}$, while the average spacing between two modes is given by $\Delta\lambda_T = 0.105\,\text{nm}$ ($\Delta f_T = 21.40\,\text{GHz}$).

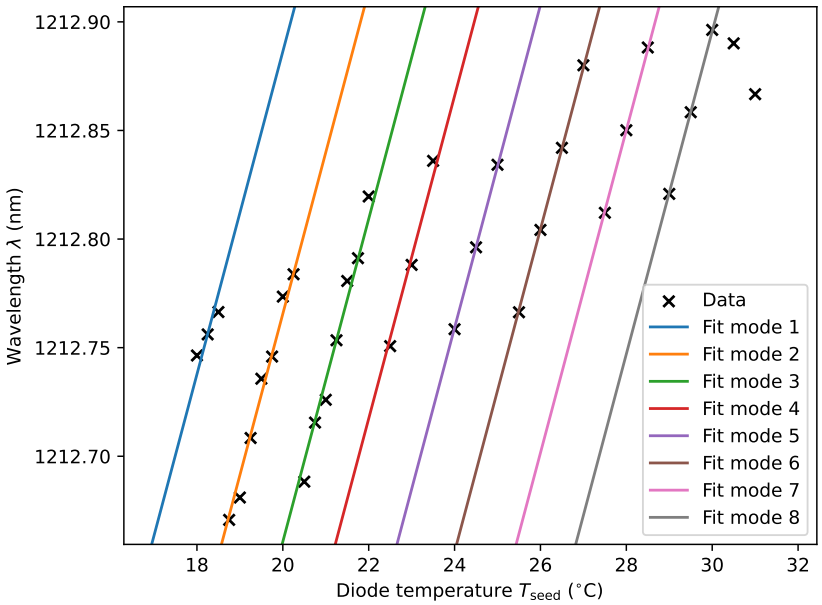

Figure 3.5: Measured wavelength λ as a function of diode temperature T_{seed} of the seed laser of the cooler. The wavelength of a mode rises linearly with the diode temperature. The average wavelength that can be tuned over before a mode jump occurs is $\Delta\lambda_T = 0.105\,\text{nm}$. The average gain of the modes is $0.074\,\text{nm}/°\text{C}$.

3.1.3 Characterization of the amplifying and frequency-doubling stage

All components of the amplifying and frequency-doubling (VRFA) stage are shown in Figure 3.2. Their properties are characterized in this subsection.

The efficiency of phase-matching directly impacts the output power of the VRFA. The output power as a function of the crystal temperature[6] is shown in Figure 3.6.

The highest output power is achieved at $T_{\text{opt}} = 65.5\,°\text{C}$. This measurement was performed at an input power of $P_{\text{seed}} = 15\,\text{W}$. However, the characteristics of the $P(T)$-graph are independent of the seed power. The performance of the frequency-doubling stage at a seed power of $P_{\text{seed}} = 36\,\text{mW}$ at the optimal temperature T_{opt} is shown in Figure 3.7.

The VRFA stage starts emitting light at a pump current of $I_{\text{th}} = 2700\,\text{mA}$. The power then increases exponentially before becoming linear. The maximum power according to the data sheet is $P_{\text{max,data sheet}} = 2.5\,\text{W}$ at an input current of $I = 4.85\,\text{A}$ [50]. The highest measured powers here are $P_{\text{max,PM}} = 1128\,\text{mW}$ and $P_{\text{max,VRFA}} = 1432\,\text{mW}$ at $I = 4700\,\text{mA}$. The VRFA system measures the output power internally and displays it on the GUI. The actual power detected externally is measured with the power meter. This explains their

[6]The temperature is measured with the VRFA system.

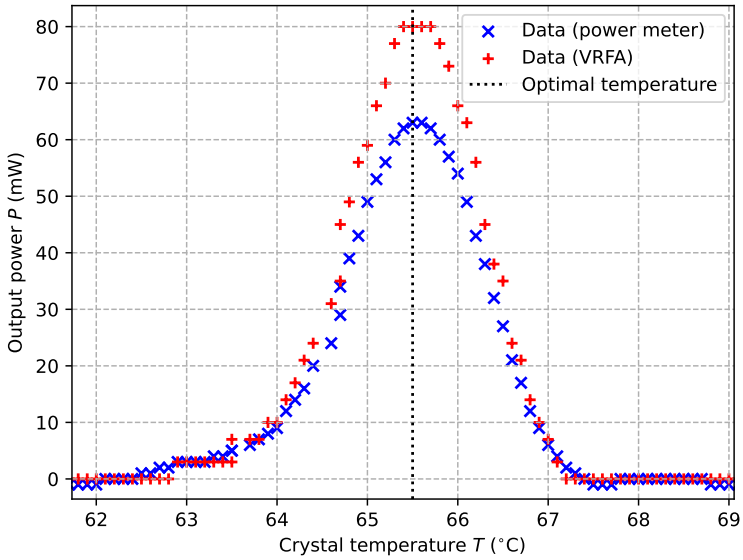

Figure 3.6: Measured output power P of the frequency-doubling stage of the cooler as a function of the temperature T of the built in SHG crystal. The maximum is at $T_{\text{opt}} = 65.5\,°\text{C}$. The output powers are measured with a power meter and with the VRFA system.

discrepancy, since the beam has to propagate through some optical components before being outcoupled. Possible factors that influence the power in general are a bad mode of the seed laser or inefficient fiber coupling. The maximum power can be increased by increasing the seed power. Intuitively, if more photons with the same frequency are coupled into the amplifier more Raman scattering processes will take place which leads to a higher output power. Figure 3.8 shows the performance at a seed power of $P_{\text{seed}} = 50\,\text{mW}$. At this input power the maximum powers are $P_{\text{max,PM}} = 1590\,\text{mW}$ and $P_{\text{max,VRFA}} = 1770\,\text{mW}$ at $I = 4800\,\text{mA}$. The form of the curve of this measurement remains the same as before with less seed power.

Figure 3.9 shows the output power P as a function of the seed power P_{seed} at $T_{\text{opt}} = 65.5\,°\text{C}$ and constant pump current $I = 3500\,\text{mA}$. In Figure 3.9, there are power intervals in which the output power seems to plateau. The first plateau is in the range between 8 mW and 18 mW, the second plateau in the range between 22 mW and 32 mW and the third plateau in the range between 38 mW and 46 mW. The transitions between the plateaus are characterized by dips in output power. The dips are due to bad modes of the seed laser, in which multiple frequencies are emitted at the same time. Any given frequency component must exceed a certain threshold power to be amplified by the VRFA. Thus, when the seed

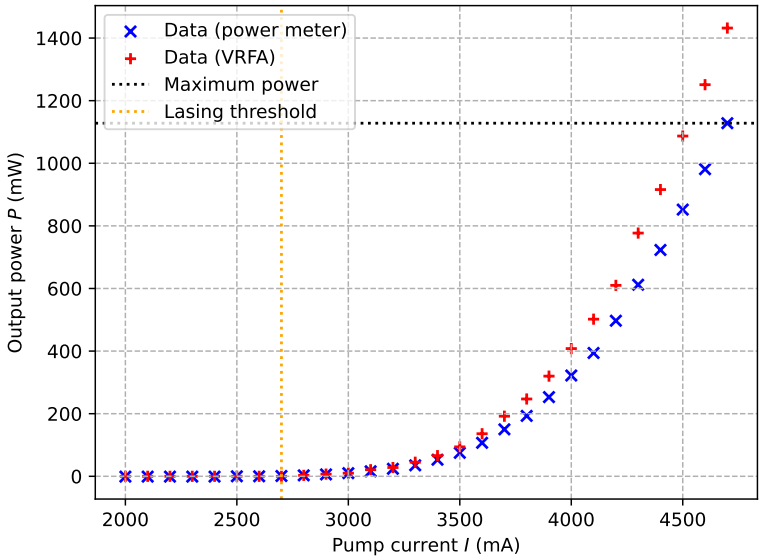

Figure 3.7: Measured performance of the VRFA of the cooler at the constant seed power of $P_{\text{seed}} = 36\,\text{mW}$. The output powers are measured with a power meter and with the VRFA system.

laser is at a bad mode, parts of the seed power will not be amplified and are lost. Therefore the emitted power decreases when the seed laser changes to a bad mode. Since the seed power is increased by increasing the current of the seed laser, different modes naturally occur as shown in Figure 3.4[7].

The beam profile of the SHG outcoupler of the cooler is shown in Figure 3.10. The beam waist of the cooler is $w_0 = 468\,\mu\text{m}$ and is 27 cm away from the outcoupler.

[7]Only the wavelength of the mode with most power is shown. Other wavelengths can be emitted too at bad modes.

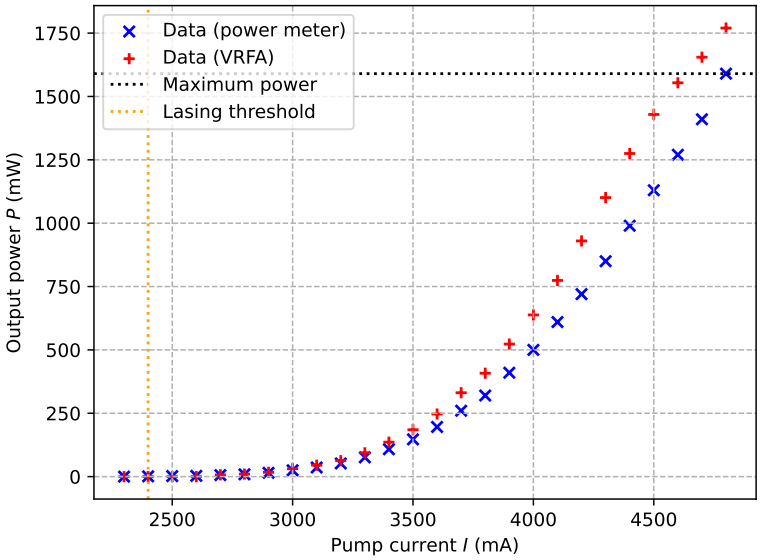

Figure 3.8: Measured performance of the VRFA of the cooler at the constant seed power of $P_{\text{seed}} = 50\,\text{mW}$. The output powers are measured with a power meter and with the VRFA system.

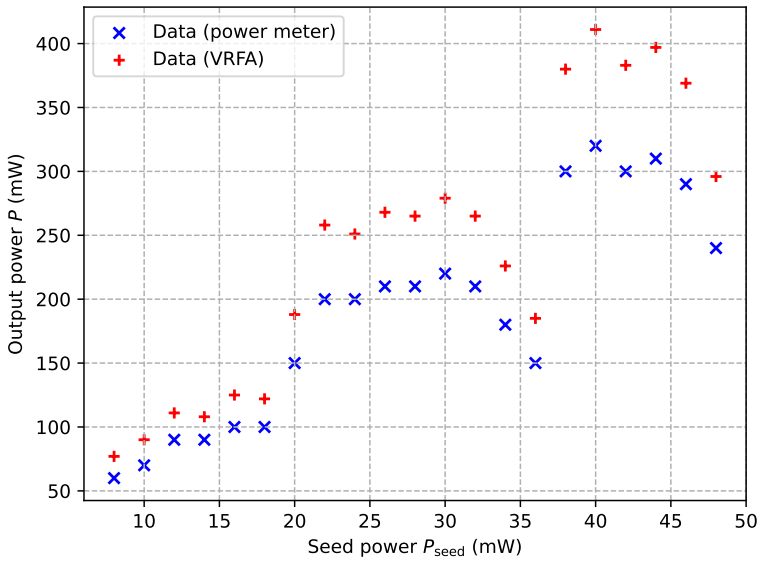

Figure 3.9: Measured output power of the VRFA of the cooler as a function of the seed power at $T_{\text{opt}} = 65.5\,^{\circ}\text{C}$ and a constant pump current $I = 3500\,\text{mA}$. The dips in the areas of $P_{\text{seed}} = 18\,\text{mW}$, $36\,\text{mW}$ and $48\,\text{mW}$ are due to bad modes of the seed laser. If the seed laser is at a bad mode not all frequencies emitted will be amplified and some of the power is lost.

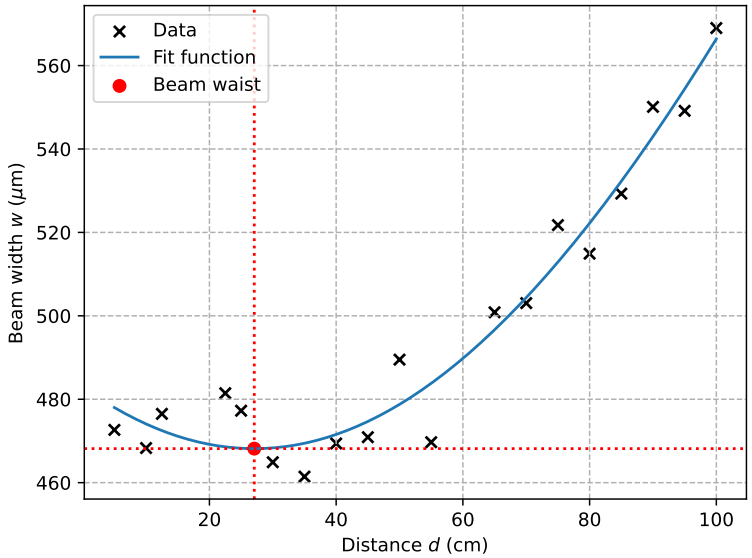

Figure 3.10: Measured beam profile of the cooler. The waist $w_0 = 468\,\mu$m is 27 cm behind the outcoupler. The fit function is based on equation (2.3.5).

3.2 First repumper

3.2.1 Setup of the first repumper

The setup of the first repumper is analogous to the setup of the cooler. The seed laser is a diode laser[8] with the wavelength $\lambda = 1257.2\,$nm. It is fiber coupled into its amplifying and frequency-doubling stage (VRFA). The output light has the wavelength $\lambda = 628.6\,$nm and we aim for powers up to 2 W.

3.2.2 Seed laser characterization

The seed laser can be tuned to a wavelength in the range between 1227.56 nm and 1285.64 nm [51]. Before any characterization measurements were done this laser was tuned to 1256 nm (238.69 THz) by adjusting the grating. The characterization measurements and their evaluation process of this seed laser are the same as for the seed laser of the cooler described in subsection 3.1.2.

The performance of the seed laser of the first repumper at constant diode temperature $T_{\text{seed}} = 20\,^{\circ}$C is shown in Figure 3.11. The lasing threshold is $I_{\text{th}} = 53.4\,$mA and the slope

[8] *TOPTICA Photonics DL pro*

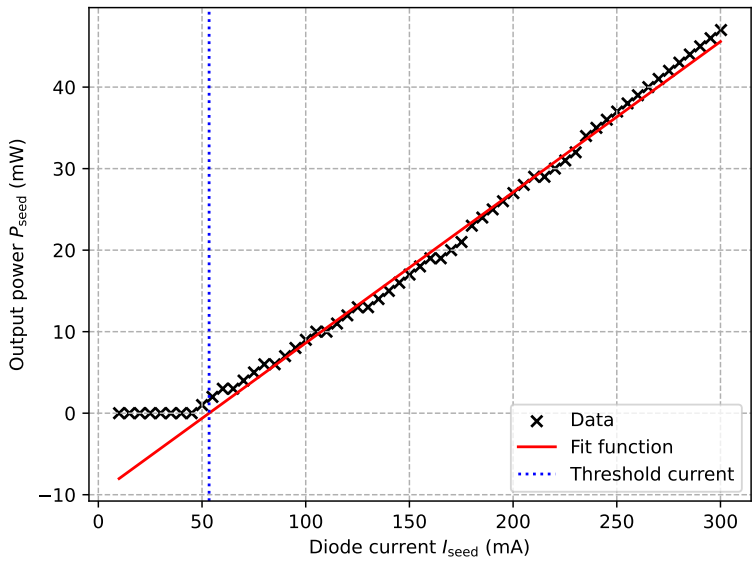

Figure 3.11: Measured output power of the 1256 nm diode laser of the first repumper as a function of the diode current. The lasing threshold is at 53.4 mA and the slope efficiency is 0.285 mW/mA.

efficiency is 0.285 mW/mA. Furthermore the maximum power measured in this measurement is $P_{\max} = 47.0\,\text{mW}$ at $I_{\max} = 300\,\text{mA}$. The data sheet lists the lasing threshold at $I_{\text{th,data sheet}} = 51.0\,\text{mA}$, the slope efficiency at $m_{\text{data sheet}} = 0.434\,\text{mW/mA}$ and the maximum power $P_{\text{max,data sheet}} = 108.3\,\text{mW}$ at the maximum diode current $I_{\text{max,data sheet}} = 300\,\text{mA}$ [51]. The reasons for the deviations between the measurements performed here and the data sheet are the same as pointed out in subsection 3.1.2.

Figure 3.12 shows the wavelength as a function of the current at a constant temperature $T = 20.0\,°\text{C}$. In this plot three different modes are visible. The mode jumps appear when the current is increased above a critical value. However, the laser runs mode-hop free over a range of approximately 0.025 nm, which corresponds to a frequency range of 4.75 GHz, which is more than enough for sufficient fine tuning.

Figure 3.13 shows the wavelength as a function of the diode temperature at constant diode current $I_{\text{seed}} = 200\,\text{mA}$. An increase in the diode temperature causes the output wavelength to change, because the resonance wavelength of the diode resonator changes. This can lead to mode jumps. Here, five different modes with equal or more than three data points are visible. The average gain of the modes is given by $m_{\lambda,T} = 0.045\,\text{nm}/°\text{C}$.

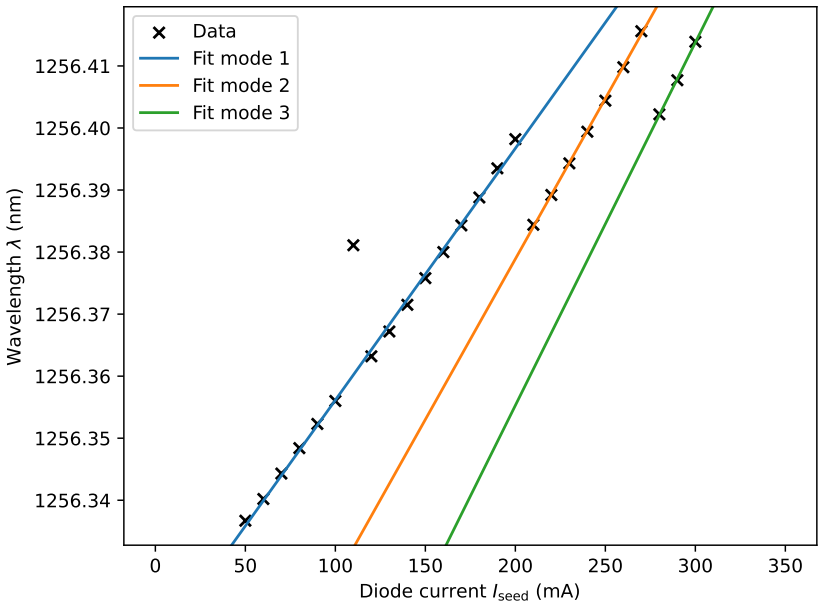

Figure 3.12: Measured wavelength λ as a function of diode current I_{seed} of the seed laser of the first repumper. The wavelength of a mode rises linearly with the diode current.

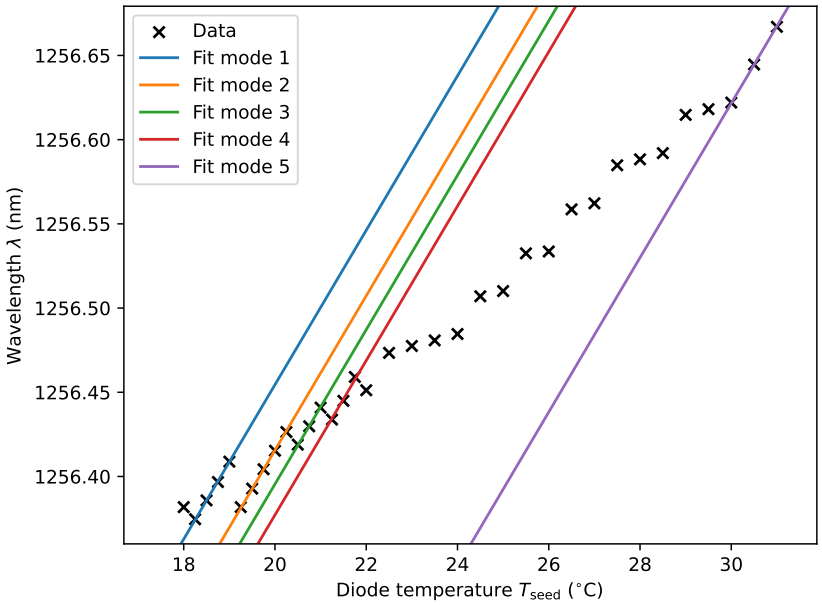

Figure 3.13: Measured wavelength λ as a function of diode temperature T_{seed} of the seed laser of the first repumper. The wavelength of a mode rises linearly with the diode temperature. The average gain of the modes is 0.045 nm/°C.

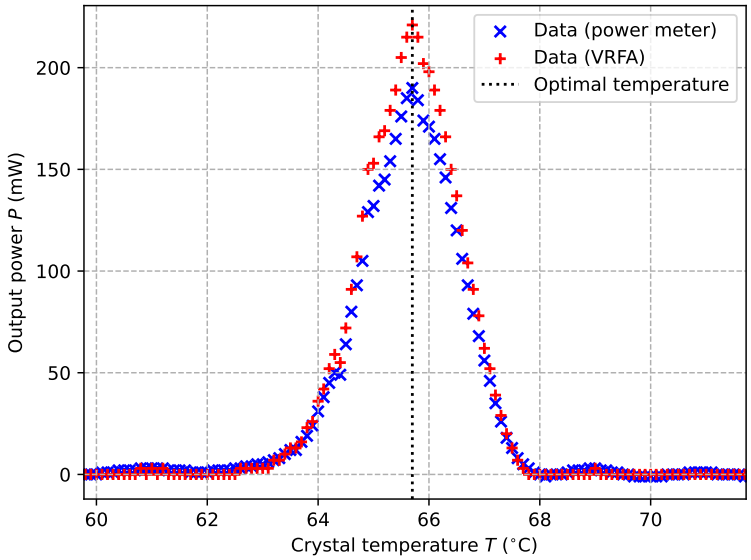

Figure 3.14: Measured output power P of the frequency-doubling stage of the first repumper as a function of the temperature T of the built in SHG crystal. The maximum is at $T_{\text{opt}} = 65.7\,°\text{C}$. The output powers are measured with a power meter and with the VRFA system.

3.2.3 Characterization of the amplifying and frequency-doubling stage

All characterization measurements and their evaluation process of this amplifying and frequency-doubling stage (VRFA) are the same as for the VRFA system of the cooler described in subsection 3.1.3.

The output power as a function of the SHG crystal's temperature is shown in Figure 3.14. The input seed power was $P_{\text{seed}} = 29\,\text{mW}$, while the pump current of the VRFA system was set to $I = 3700\,\text{mA}$. The highest power emitted is at $T_{\text{opt}} = 65.7\,°\text{C}$.

The performance of the frequency-doubling stage at a seed power of $P_{\text{seed}} = 28\,\text{mW}$ at T_{opt} is shown in Figure 3.15. The laser starts emitting light at a current of $I_{\text{th}} = 2497\,\text{mA}$. The maximum power according to the data sheet is $P_{\text{max,data sheet}} = 2.4\,\text{W}$ at an input current of $I = 5.3\,\text{A}$ [52]. The maximum powers are $P_{\text{max,PM}} = 2110\,\text{mW}$ and $P_{\text{max,VRFA}} = 2317\,\text{W}$ at $I = 5300\,\text{mA}$.

Figure 3.16 shows the output power P as a function of the seed power P_{seed} at $T_{\text{opt}} = 65.7\,°\text{C}$ and constant pump current $I = 4000\,\text{mA}$. The output power rises continuously with increasing seed power.

The beam profile of the outcoupler of the first repumper is shown in Figure 3.17. The beam waist of the first repumper is $w_0 = 460\,\mu\text{m}$ and is 17 cm away from the outcoupler.

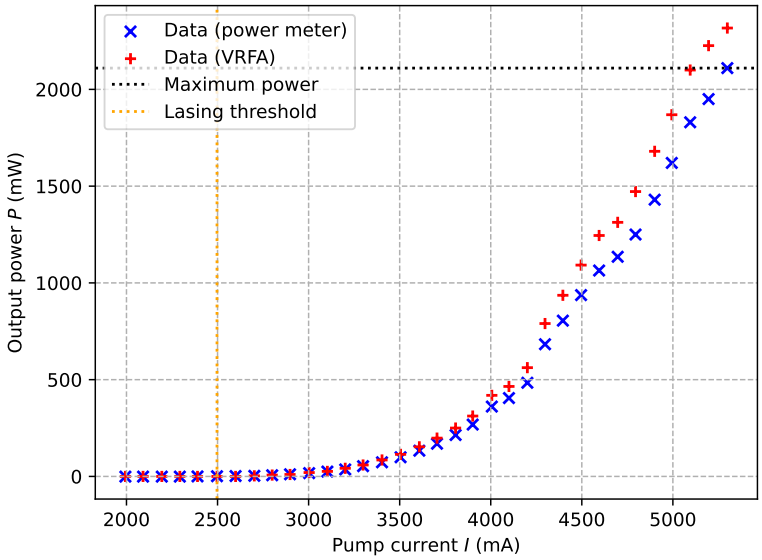

Figure 3.15: Measured performance of the VRFA system of the first repumper at the constant seed power of $P_{\text{seed}} = 28\,\text{mW}$. The output powers are measured with a power meter and with the VRFA system.

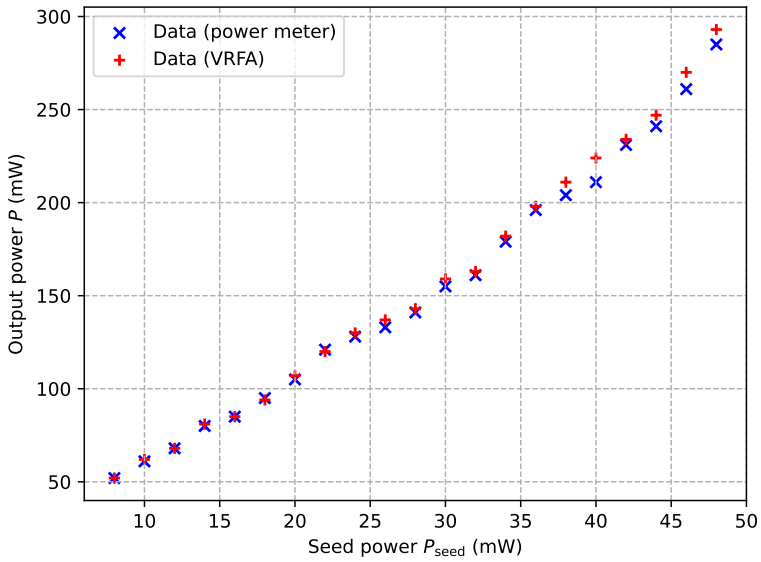

Figure 3.16: Measured output power as a function of the seed power at $T_{\text{opt}} = 65.7\,°\text{C}$ and a constant pump current $I = 4000\,\text{mA}$ for the first repumper. The output power increases linearly with the seed power.

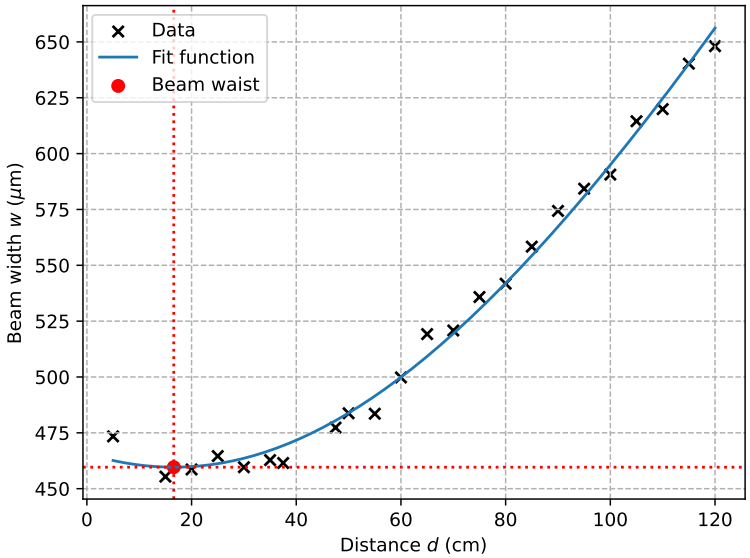

Figure 3.17: Measured beam profile of the first repumper. The waist $w_0 = 460\,\mu$m is 17 cm behind the outcoupler. The fit function is based on equation (2.3.5).

3.3 Second repumper

The second repumper needs to powers of order 60 mW at a wavelength of $\lambda = 628.1$ nm [29, 33]. In this experiment, this is achieved with a diode laser. There are no laser diodes made for this specific wavelength, but there are some for $\lambda \approx 632$ nm which can, under suitable conditions, operate at the desired 628.1 nm.

Unfortunately, due to delivery problems caused by the pandemic the manufacturer has so far not been able to deliver the diode. For this reason, only the body of the laser has been designed and assembled, as described below.

The second repumper requires much less output power than the first repumper. So, for the second repumper we opted for a home-built laser system based on a design that was developed previously at our institute. Figure 3.18a is a photograph of the general setup of the an institute-made diode laser. In Figure 3.18b a photograph of the current status of the second repumper is shown. The laser diode is mounted in the diode holder. The adjustable lens block with a collimation lens is placed in front of it. The grating provides feedback for the diode. A part of the emitted light from the diode is reflected back into it, leading to stimulated emission. Another part of the light is diffracted out of the cavity. The angle of the grating is adjusted with a screw and a piezo for rough and fine tuning respectively. A Peltier element is mounted under the base plate to stabilize the temperature of the laser diode. Sensors ensure control over the diode current, diode temperature and the grating

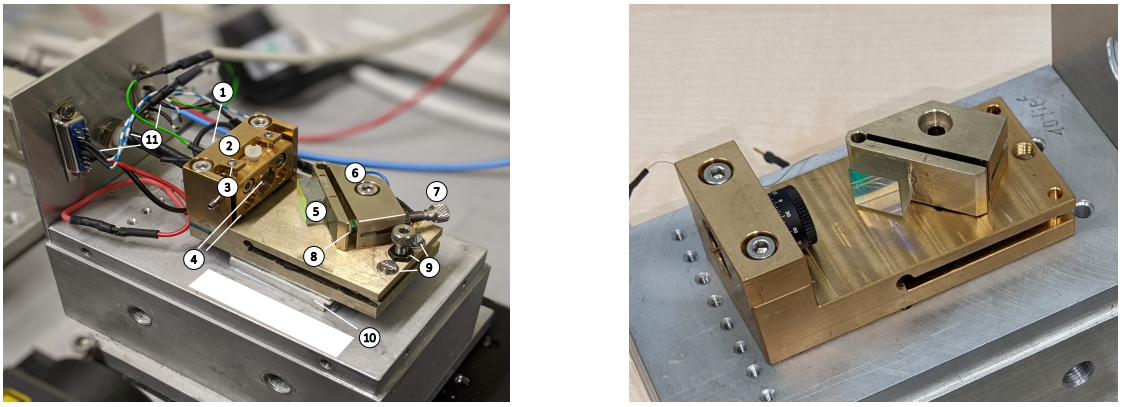

(a) (b)

Figure 3.18: (a) Photograph of the interior of an institute-made diode laser. [1] Laser diode [2] Diode holder [3] Screws for adjustment of the lens block [4] Lens and lens block [5] Grating [6] Grating holder [7] Screw for grating angle adjustment [8] Piezo for fine-tuning of the grating angle [9] Screws for vertical grating alignment [10] Peltier element [11] Ports for current, temperature and piezo control. (b) Photograph of current status of the second repumper.

angle.

The grating of this laser has a line spacing of $d = 5.6 \cdot 10^{-7}\text{m}$. The Littrow angle α_L in the first order for the wavelength $\lambda = 628.1\,\text{nm}$ is given by

$$\alpha_L = \arcsin\left(\frac{\lambda}{2d}\right) = \arcsin\left(\frac{628.1 \cdot 10^{-9}\text{m}}{2 \cdot 5.5 \cdot 10^{-7}\text{m}}\right) \approx 34.42\,^\circ\,. \tag{3.3.1}$$

3.4 Locking

Setup We use a scanning transfer cavity lock to stabilize the frequency of the cooler and the first repumper. The cavity is an institute-made plano-concave cavity with a length of $L = 15\,\text{cm}$. The concave mirror has a curvature of $\mathcal{R}_2 = 20\,\text{cm}$. In order to couple the cooler and repumper beams into the cavity, the beams have to be mode-matched to the cavity. The parameters for an ideal coupling are given in Table 3.1. The curvature of a beam has to match the curvature of both mirrors, as described in subsection 2.3.5.

In the lock, we use a frequency-stabilized helium-neon laser (HeNe)[9] as a frequency reference. It operates at a wavelength of 632.8 nm and has a frequency stability of $\pm 2.5\,\text{MHz}$ over 24 h [53]. When the lock is activated, the feedback from a *Red Pitaya*[10] keeps the

[9] *SIOS Meßtechnik, Stabilisierte He-Ne-Laser Serie SL 04*
[10] A *Red Pitaya* is a FPGA board.

Table 3.1: Ideal parameters for locking the cooler and first repumper to the helium-neon laser (HeNe). The distance between the outcoupler of a laser and its position of the beam waist is given by d_0.

Parameter	**HeNe**	**Cooler**	**First repumper**
d_0 [cm]	19.36	27.08	16.60
w_0 [μm]	326.98	468.15	459.62
z_0 [m]	0.53	1.08	1.05
w_1 [μm]	132.08	129.25	131.57
f [m]	0.23	0.31	0.31

transmission peaks at a constant distance from each other. Especially, it individually keeps the peaks from the cooler and first repumper at a constant distance to the peak from the HeNe. Thus the cooler and first repumper are kept at a constant frequency.

The positions of the waist of the beams after the outcoupler d_0 and the waists w_0 of the beams were measured with a beam profiler[11]. Figure 3.19 shows the beam profiles of the HeNe, the cooler ($\lambda = 606.3\,\text{nm}$) and the first repumper ($\lambda = 628.6\,\text{nm}$).

The required beam waist at the position of the planar mirror of the beam w_1 is given by equation (2.3.29). A thin lens is included in the setup to satisfy this condition. The focal length f of the thin lens is derived from equation (2.3.11) is given by

$$f = \frac{z_0}{\sqrt{\left(\frac{w_0}{w_1}\right)^2 - 1}}. \tag{3.4.1}$$

Figure 3.20 shows the locking scheme. The lenses optimally should have the focal lengths $f_0 = 23\,\text{cm}$, $f_1 = 31\,\text{cm}$ and $f_2 = 31\,\text{cm}$. In our setup we use lenses with $f_0 = 20\,\text{cm}$, $f_1 = 30\,\text{cm}$ and $f_2 = 20\,\text{cm}$. The mode-matching is good enough for a high-finesse coupling despite this slight mismatch. The lenses are positioned such that their focal planes are aligned with the planar mirror. The laser outcouplers are positioned so that the beams' waists are in the focal plane of the lenses. The cavity length is varied by a piezoelectric element. Different resonances are visible on the photo diode (PD) signal, depending on the current resonator length. Each of these resonances can be matched to a frequency. The photo diode sends the signal to a *Red Pitaya* which adjusts the diode current of the cooler and of the first repumper according to a stabilization protocol developed at our institute [54].

Demonstration of locking two lasers with one cavity Depending on the finesse of the cavity, more than one laser can be locked with the transfer cavity scheme. In our setup

[11] *Dataray WinCamD-LCM-1" CMOS*

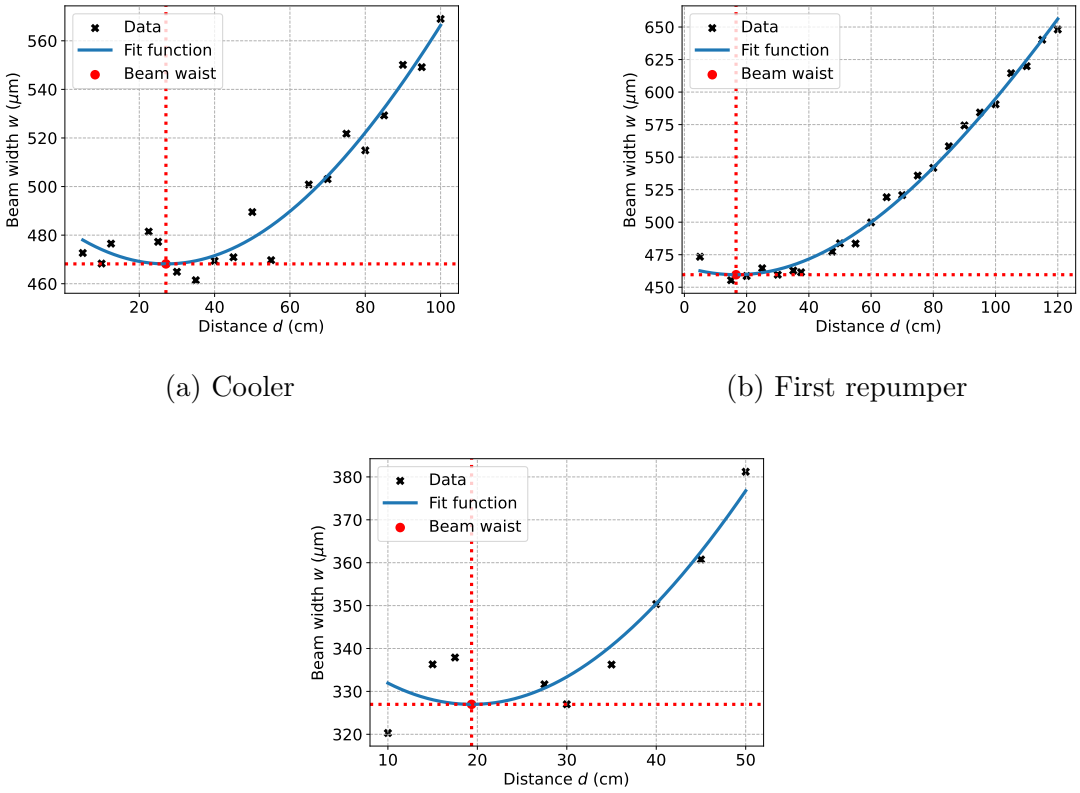

(a) Cooler

(b) First repumper

(c) Helium-neon laser

Figure 3.19: Beam profiles measured with the beam profiler to determine the waist size as well as the waist position.

we lock the cooler and the first repumper on the same cavity. Figure 3.21a shows the peak positions of the lasers on the cavity during locking. Some higher Gaussian modes are also visible as smaller peaks. The fluctuations of the cavity shift all laser peaks equally, so it does not affect their relative distance. However, fluctuations of external factors like temperature or air pressure induce frequency fluctuations of the lasers' seed lasers. These frequency fluctuations in turn cause fluctuations of the peak positions of the lasers. Hence error signals of the lasers arise, because their peak positions deviate from their desired values. The aforementioned fluctuations of the cavity influence the absolute position of the HeNe peak. These resulting deviations are tracked by the error signal of the HeNe. The error signals of all three lasers are shown in Figure 3.21b.

The lock keeps the frequency of both slave lasers constant over a time span of 25 min. While the lock is active, the lasers' frequency stays in a range of ±2 MHz. The standard deviations σ of the error signals, pictured in Figure 3.21b, are $\sigma_{\mathrm{HeNe}} = \pm 0.7331\,\mathrm{MHz}$,

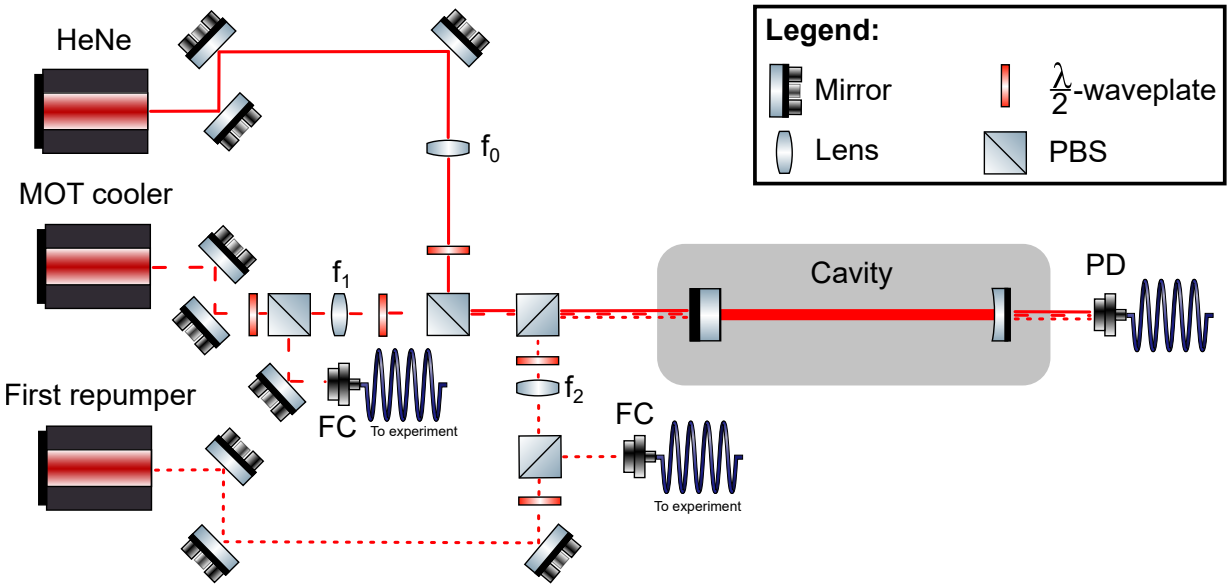

Figure 3.20: Locking scheme for frequency stabilization of the cooler and the first repumper. The photo diode (PD) signal is sent to a computer which then provides feedback to the lasers. The cooler and the first repumper beams are fiber coupled (FC) and through these fibers the light is brought to the experimental setup.

$\sigma_{606} = \pm 0.4872\,\text{MHz}$ and $\sigma_{628} = \pm 0.5778\,\text{MHz}$. A typical histogram of such an error signal is shown in Figure 3.21c. The error and thus the lasers' frequency does not fluctuate much. Since the natural linewidth of the $A^2\Pi_{1/2}$ state is 8.29 MHz, the frequency fluctuations are small enough to be tolerated.

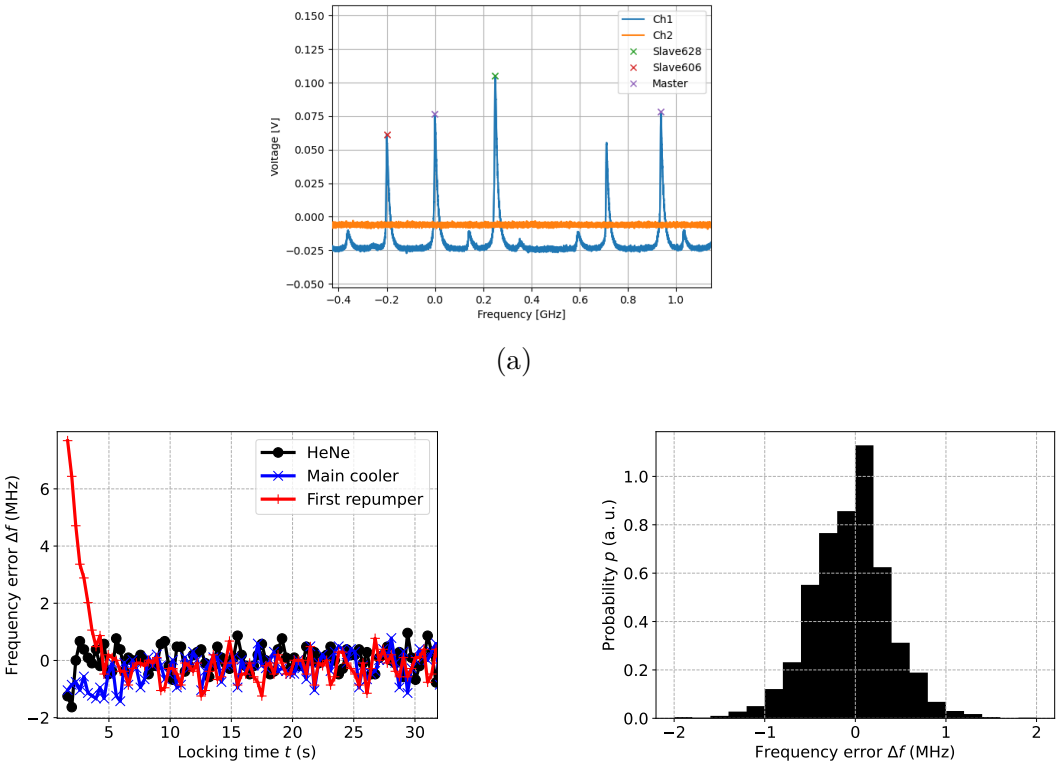

Figure 3.21: Measured peak positions and error signals while locking. (a) Screenshot of the scanning cavity lock program [54]. In the photo diode signal (blue) a series of three large peaks is apparent. This series repeats when the piezo voltage is scanned, which is why similar peaks appear in the right half of the plot. These peaks signify the fundamental mode of the HeNe (Master), the cooler (Slave606) and the first repumper (Slave628). Their positions remain constant relative to each other while the lock is active. (b) Error signals of the positions of the individual peaks. This signal is given as feedback to the locking program which then processes it and adjusts the diode currents of the seed lasers of the slave lasers accordingly. (c) Histogram of the error of the first repumper. The standard deviation is $\sigma_{628} = \pm 0.5778\,\mathrm{MHz}$.

3.5 Dipole trap laser

In the overall experiment, the molecular ensemble will be cooled lower than the Doppler limit via evaporative cooling. Therefore the molecules are trapped in a conservative trap. An example of such a conservative trap is an optical dipole trap. Equation (2.2.6) is a good approximation of such a potential. The laser has to be far red detuned from the transition frequencies in order to have an attractive force towards the trap's center while at the same time minimizing the scattering rate of the photons of the dipole trap beam. The smallest transition frequency of a transition involving the X(0) state is the X(0)-A(0) transition with a frequency of $\omega_0 = 494.43\,\mathrm{THz}$. The dipole laser used in this experiment has a wavelength of $\lambda = 1064\,\mathrm{nm}$ or $\omega_{\mathrm{dip}} = 281.75\,\mathrm{THz}$, very far detuned from the X(0)-A(0) transition.

Suppose that the dipole trap is loaded with an ensemble at the Doppler temperature $T_{\mathrm{D}} = 198.93\,\mu\mathrm{K}$ and that the dipole trap laser beam has a beam waist of $w_0 = 200\,\mu\mathrm{m}$. Inserting the intensity profile of a Gaussian beam (equation (2.3.9)) into equation (2.2.6) at the trap center ($\mathbf{r} = \mathbf{0}$) leads to a condition for the intensity I_0 of the dipole laser beam. The intensity required to create a dipole trap potential with a trap depth of $k_B T_{\mathrm{D}}$ is

$$I_0 = k_{\mathrm{B}} T_{\mathrm{D}} \cdot \frac{2\omega_0^3}{3\pi c^2} \frac{\Delta}{\Gamma}. \tag{3.5.1}$$

Typically, dipole traps are operated at two to three times the required trap depth [55–57]. In the experiment this results in a required intensity of $I_0 = 21\,\mathrm{kW/cm^2}$. In order to reach such high intensities on a area of the cross-section of the Gaussian beam at the waist, the laser beam has to have a power of 26.4 W.

In this experiment these high powers are reached by a commercial laser with an ytterbium-doped fiber[12]. The maximum power this laser can provide is 46.5 W [58].

3.5.1 Power stability of the laser

The dipole laser has to emit light at constant power to make sure that the dipole potential is not noisy. A noisy potential can lead to excitations of the trapped molecules which results in heating. This ultimately does not only lead to loss of molecules and lower densities, but also directly prevents reaching lower temperatures and thus creating a Bose-Einstein condensate.

Measuring the drift in laser power was done by directing the beam into a high power meter head[13]. The laser power emitted was tuned to approximately 34 W because of power limitations of the high power meter head.

Figure 3.22 shows the power of the dipole laser over 5 hours. The mean power during this measurement was $\langle P \rangle = 34.1\,\mathrm{W}$ with a standard deviation of $\sigma = 53.2\,\mathrm{mW}$. This

[12] Azurlight Systems ALS-IR-1064-50-I-CP-SF

[13] The power meter is a *Thorlabs PM100A* and the head a *Thorlabs S314C*.

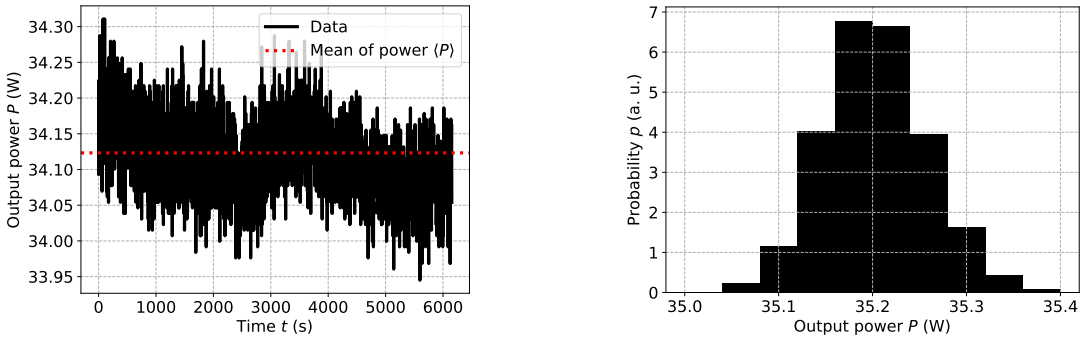

(a) (b)

Figure 3.22: Power stability over time of the dipole trap laser. (a) The power drifts slightly over 90 minutes. (b) Histogram of the power. The mean power is $\langle P \rangle = 34.1\,\mathrm{W}$ with a standard deviation of $\sigma = 53.2\,\mathrm{mW}$. This converts to a stability of $\pm 0.16\%$.

leads to fluctuations of $\pm 0.16\%$ in power which satisfies the requirements. These small fluctuations are small enough that they will only influence the dynamics in the dipole trap in a negligible manner.

3.5.2 Outlook: Power stabilization of short term fluctuations

The long term fluctuations do not hinder the evaporative cooling process. However, the short term fluctuations, which can be seen in the overall noisy signal depicted in Figure 3.22a could have a detrimental impact on the dynamics of a trapped ensemble by exciting molecules [59]. Figure 3.23 shows a scheme how short term fluctuations of the dipole trap laser's power could be compensated [60, 61]. This setup exploits the fact that the intensity of the first diffraction order of an acousto-optical modulator (AOM) depends on the intensity of the applied RF signal.

All but one of the diffracted orders are blocked by an iris. Here the 1st diffracted order is transmitted. A glass plate reflects a small amount of the intensity of the laser into a photo diode. The power is measured and processed by feedback electronics. They will adjust the input intensity at the AOM so that the power of the 1st order of the light beam remains constant.

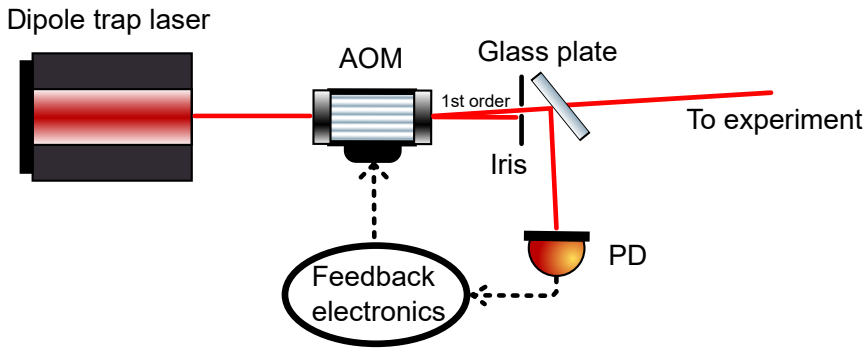

Figure 3.23: Power stabilization scheme with an acousto-optic modulator (AOM). The photo diode (PD) measures the power. Feedback electronics will then regulate the intensity of the RF input of the AOM. This adjusts the power of the light beam accordingly.

3.5.3 Outlook: Radial and axial trap frequencies for a single beam dipole trap

The optical dipole trap's potential, which is given by equation (2.2.6), can be well approximated by an harmonic potential close to the trap center. The intensity profile of a Gaussian beam (see equation (2.3.9)) then leads to the relation

$$\frac{1}{2}m(\omega_\rho^2\rho^2+\omega_z^2z^2)+C=-\frac{3\pi c^2}{2\omega_0^3}\frac{\Gamma}{\Delta}I_0\left(\frac{w_0}{w(z)}\right)^2\cdot\exp\left(-\frac{2\rho^2}{w^2(z)}\right), \tag{3.5.2}$$

where on the left of the equation m is the mass of the molecule, ρ and z the radial and axial coordinates, ω_ρ and ω_z their angular frequency and C a constant. On the right of the equation is c the speed of light, ω_0 the transition frequency of the closest transition to the dipole trap laser's frequency [11], Γ the linewidth of the excited state of the same transition, Δ the detuning of the dipole trap laser, I_0 the maximum intensity of the Gaussian beam and w_0 the beam waist, while $w(z)$ describes the beam width.

In order to calculate the radial trap frequency z is set to zero. A Taylor expansion up to second order of the exponential function then leads to the expression

$$\omega_\rho=\sqrt{\frac{6\pi c^2}{\omega_0^3w_0^2m}\frac{\Gamma}{\Delta}I_0}. \tag{3.5.3}$$

The axial trap frequency can be calculated by setting $\rho=0$ and approximating the beam width for small z as $w(z)\approx 1-\left(\frac{z}{z_0}\right)^2$, with z_0 being the Rayleigh length. This then leads to

$$\omega_z=\sqrt{\frac{3\pi c^2}{\omega_0^3mz_0^2}\frac{\Gamma}{\Delta}I_0}. \tag{3.5.4}$$

The mass of CaF is $m = 59\,\mathrm{u}$. The closest transition in our transition scheme depicted in Figure 2.3 to the frequency of the dipole trap laser is the X(0)-A(0) transition, hence $\omega_0 = 494.43\,\mathrm{THz}$ [33]. The Rayleigh length of the dipole trap laser is given by equation (2.3.8), where $\lambda = 1064\,\mathrm{nm}$. The linewidth of the A state is $\Gamma = 8.29\,\mathrm{MHz}$ [29]. The detuning of the dipole trap laser is $\Delta = 212.68\,\mathrm{THz}$. Additionally it is assumed that the power of the dipole trap laser is $P = 45\,\mathrm{W}$ and is then focused on a circular area with the radius $w_0 = 200\,\mu\mathrm{m}$. Inserting these parameters into equations (3.5.3) and (3.5.4) leads to

$$\omega_\rho = 2\pi \cdot 1096\,\mathrm{Hz} \quad \text{and} \quad \omega_z = 2\pi \cdot 1.3\,\mathrm{Hz}.$$

Thus we can achieve strong radial confinement in our dipole trap. If the axial trap proves to have insufficient confinement, it is possible to create a crossed dipole trap instead, where the weak axial confinement of one beam is compensated by the strong radial confinement of the other.

4 Conclusion & outlook

In this thesis, two laser systems for the laser cooling and magneto-optical trapping of calcium monofluoride (CaF) have been set up, characterized and frequency stabilized. A third laser system has been designed and constructed for the same purpose. Moreover, the dipole trap laser has been set up and characterized.

The lasers which were set up and characterized were the cooler, operating on the $X^2\Sigma^+(\nu = 0) \longrightarrow A^2\Pi_{1/2}(\nu = 0)$ transition of CaF, and the first repumper, operating on the $X^2\Sigma^+(\nu = 1) \longrightarrow A^2\Pi_{1/2}(\nu = 0)$ transition. The cooler emits light at 606.3 nm (494.46 THz) with output powers up to 1.6 W and is tunable over a range of 0.05 nm (40.77 GHz) without mode jumps. The first repumper emits light at 628.6 nm (476.92 THz) with output powers up to 2.1 W and is tunable over a range of 0.01 nm (7.59 GHz) without mode jumps. Using a scanning transfer cavity lock [54], both lasers were frequency stabilized on the same cavity for over 25 minutes. Later in the experiment they will be locked for several hours. In the next step, sidebands have to be applied to the lasers to address the hyperfine structure of the ground state of CaF. The beam source that is needed for the production of the CaF molecules is currently under construction. With the newly set up lasers and the existing $X^2\Sigma^+(\nu = 0) \longrightarrow B^2\Sigma^+(\nu = 0)$ slowing laser [34] it is now possible to slow and cool the molecular beam.

The second repumper, operating on the $X^2\Sigma^+(\nu = 2) \longrightarrow A^2\Pi_{1/2}(\nu = 1)$ transition of CaF, was designed and partially constructed. The only part missing from this laser is the laser diode at 628.1 nm (477.30 THz). Once this laser is complete, better slowing and cooling of the molecules will be possible, because a molecule will be able to scatter more than 10^4 photons before decaying to a state that is not addressed by a laser.

Furthermore, the dipole trap laser at 1064 nm (281.76 THz) has been set up and characterized. The power stability of the dipole trap laser has been measured and a scheme for the power stabilization has been proposed. The minimum power needed for this conservative trap has been calculated to be 25 W, and the dipole trap laser exceeds this minimum with a maximum output power of 46.5 W.

In conclusion, the laser systems that have been set up and characterized during the course of this thesis are a crucial component of the new CaF experiment. The setup of the molecular source will begin in the near future. With these developments, the way is paved for the first creation and observation of a molecular beam in the new experiment. This is another important step of working towards the creation of a molecular Bose-Einstein condensate.

Bibliography

[1] A. Ashkin, *Acceleration and Trapping of Particles by Radiation Pressure*, Phys. Rev. Lett. **24**, 4 (1970), pp. 156–159,
URL: https://doi.org/10.1103/PhysRevLett.24.156

[2] A. Ashkin, *Atomic-Beam Deflection by Resonance-Radiation Pressure*, Phys. Rev. Lett. **25**, 19 (1970), pp. 1321–1324,
URL: https://doi.org/10.1103/PhysRevLett.25.1321

[3] T. W. Hansch and A. L. Schawlow, *Cooling of gases by laser radiation*, Optics Communications **13**, 1 (1975), pp. 68–69,
URL: https://doi.org/10.1016/0030-4018(75)90159-5

[4] D. J. Wineland and H. Dehmelt, *Proposed* $10^{14}\Delta\nu < \nu$ *laser fluorescence spectroscopy on* TI^{+} *mono-ion oscillator III*, Bull. Am. Phys. Soc. **20**, 637 (1975)

[5] A. Ashkin, *Trapping of Atoms by Resonance Radiation Pressure*, Phys. Rev. Lett. **40** (1978), pp. 729–732,
URL: https://doi.org/10.1103/PhysRevLett.40.729

[6] D. E. Pritchard, E. L. Raab, V. Bagnato, C. E. Wieman and R. N. Watts, *Light Traps Using Spontaneous Forces*, Phys. Rev. Lett. **57**, 3 (1986), pp. 310–313,
URL: https://doi.org/10.1103/PhysRevLett.57.310

[7] S. Chu, L. Hollberg, J. E. Bjorkholm, A. Cable and A. Ashkin, *Three-dimensional viscous confinement and cooling of atoms by resonance radiation pressure*, Phys. Rev. Lett. **55**, 1 (1985), pp. 48–51,
URL: https://doi.org/10.1103/PhysRevLett.55.48

[8] P. D. Lett, W. D. Phillips, S. L. Rolston, C. E. Tanner, R. N. Watts and C. I. Westbrook, *Optical molasses*, J. Opt. Soc. Am. B **6** (1989), pp. 2084 – 2107,
URL: https://doi.org/10.1364/josab.6.002084

[9] W. D. Phillips, *Laser cooling and trapping of neutral atoms*, Reviews of Modern Physics **70**, 3 (1998), pp. 721–741,
URL: https://doi.org/10.1103/RevModPhys.70.721

[10] M. R. Tarbutt, *Laser cooling of molecules*, Contemporary Physics **59**, 4 (2018), pp. 356–376,
URL: https://doi.org/10.48550/arXiv.1902.05628

[11] R. Grimm, M. Weidemüller and Y. B. Ovchinnikov, *Optical Dipole Traps for Neutral Atoms*, Advances In Atomic, Molecular, and Optical Physics **42** (2000), pp. 95–170,
URL: https://doi.org/10.1016/S1049-250X(08)60186-X

[12] M. H. Anderson, J. R. Ensher, M. R. Matthews, C. E. Wieman and E. A. Cornell, *Observation of Bose-Einstein Condensation in a Dilute Atomic Vapor*, Science **269**, 5221 (1995), pp. 198–201,
URL: https://doi.org/10.1126/science.269.5221.198

[13] K. B. Davis, M. O. Mewes, M. R. Andrews, N. J. van Druten, D. S. Durfee, D. M. Kurn and W. Ketterle, *Bose-Einstein Condensation in a Gas of Sodium Atoms*, Phys. Rev. Lett. **75**, 22 (1995), pp. 3969–3973,
URL: https://doi.org/10.1103/PhysRevLett.75.3969

[14] S. N. Bose, *Plancks Gesetz und Lichtquantenhypothese*, Zeitschrift für Physik **26** (1924), pp. 178–181,
URL: https://doi.org/10.1007/BF01327326

[15] A. Einstein, *Quantentheorie des einatomigen idealen Gases*, Sitzungsberichte der Preussischen Akademie der Wissenschaften (1925),
URL: https://doi.org/10.1002/3527608958.ch27

[16] F. Schwabl, *Statistical Mechanics*, vol. 2 (Springer Berlin, Heidelberg, 2006),
URL: https://doi.org/10.1007/3-540-36217-7, ISBN: 9783540362173

[17] H. Haken and H. C. Wolf, *Molekülphysik und Quantenchemie*, vol. 5 (Springer Berlin, Heidelberg, 2005),
URL: https://doi.org/10.1007/3-540-30315-4, ISBN: 9783540303152

[18] Di Rosa, M. D., *Laser-cooling molecules - Concept, candidates, and supporting hyperfine-resolved measurements of rotational lines in the A-X(0,0) band of CaH*, Eur. Phys. J. D **31**, 2 (2004), pp. 395–402,
URL: https://doi.org/10.1140/epjd/e2004-00167-2

[19] E. S. Shuman, J. F. Barry and D. Demille, *Laser cooling of a diatomic molecule*, Nature **467**, 7317 (2010), pp. 820–823,
URL: https://doi.org/10.1038/nature09443

[20] S. Truppe, H. J. Williams, M. Hambach, L. Caldwell, N. J. Fitch, E. A. Hinds, B. E. Sauer and M. R. Tarbutt, *Molecules cooled below the Doppler limit*, Nature Physics

13, 12 (2017), pp. 1173–1176,
URL: http://dx.doi.org/10.1038/nphys4241

[21] J. Lim, J. R. Almond, M. A. Trigatzis, J. A. Devlin, N. J. Fitch, B. E. Sauer, M. R. Tarbutt and E. A. Hinds, *Laser Cooled YbF Molecules for Measuring the Electron's Electric Dipole Moment*, Phys. Rev. Lett. **120**, 12 (2018), p. 123201,
URL: https://doi.org/10.1103/PhysRevLett.120.123201

[22] I. Kozyryev, L. Baum, K. Matsuda, B. L. Augenbraun, L. Anderegg, A. P. Sedlack and J. M. Doyle, *Sisyphus Laser Cooling of a Polyatomic Molecule*, Phys. Rev. Lett. **118**, 17 (2017), p. 173201,
URL: https://doi.org/10.1103/PhysRevLett.118.173201

[23] L. Anderegg, B. L. Augenbraun, Y. Bao, S. Burchesky, L. W. Cheuk, W. Ketterle and J. M. Doyle, *Laser cooling of optically trapped molecules*, Nature Physics **14**, 9 (2018), pp. 890–893,
URL: https://doi.org/10.1038%2Fs41567-018-0191-z

[24] J. F. Barry, D. J. McCarron, E. B. Norrgard, M. H. Steinecker and D. Demille, *Magneto-optical trapping of a diatomic molecule*, Nature **512**, 7514 (2014), pp. 286–289,
URL: https://doi.org/10.1038/nature13634

[25] L. Anderegg, B. L. Augenbraun, E. Chae, B. Hemmerling, N. R. Hutzler, A. Ravi, A. Collopy, J. Ye, W. Ketterle and J. M. Doyle, *Radio Frequency Magneto-Optical Trapping of CaF with High Density*, Phys. Rev. Lett. **119**, 10 (2017), p. 103201,
URL: https://doi.org/10.1103/PhysRevLett.119.103201

[26] A. L. Collopy, S. Ding, Y. Wu, I. A. Finneran, L. Anderegg, B. L. Augenbraun, J. M. Doyle and J. Ye, *3D Magneto-Optical Trap of Yttrium Monoxide*, Phys. Rev. Lett. **121**, 21 (2018), p. 213201,
URL: https://doi.org/10.1103/PhysRevLett.121.213201

[27] L. Anderegg, L. W. Cheuk, Y. Bao, S. Burchesky, W. Ketterle, K.-K. Ni and J. M. Doyle, *An optical tweezer array of ultracold molecules*, Science **365**, 6458 (2019), pp. 1156–1158,
URL: https://www.science.org/doi/abs/10.1126/science.aax1265

[28] M. Schmidt, L. Lassablière, G. Quéméner and T. Langen, *Self-bound dipolar droplets and supersolids in molecular Bose-Einstein condensates*, Phys. Rev. Research **4**, 1 (2022), p. 013235,
URL: https://link.aps.org/doi/10.1103/PhysRevResearch.4.013235

[29] H. J. Williams, *Producing, trapping and controlling ultracold CaF molecules*, PhD thesis, Imperial College London (2018),
URL: https://doi.org/10.25560/62635

[30] M. Hambach, *Development of a magneto-optical trap for CaF molecules*, PhD thesis, Imperial College London (2017),
URL: https://doi.org/10.25560/54851

[31] F. Kogel, *Modeling laser cooling of diatomic molecules*, Master's thesis, University of Stuttgart (2021)

[32] N. Fitch and M. Tarbutt, *Laser-cooled molecules*, Advances In Atomic, Molecular, and Optical Physics **70** (2021), pp. 157–262,
URL: https://doi.org/10.1016/bs.aamop.2021.04.003

[33] L. G. Anderegg, *Ultracold molecules in optical arrays: From laser cooling to molecular collisions*, PhD thesis, Harvard University (2019),
URL: https://nrs.harvard.edu/URN-3:HUL.INSTREPOS:37365119

[34] O. E. Prochnow, *Setup of a Laser System for Molecular Laser Cooling*, Bachelor's thesis, University of Stuttgart (2021),
URL: https://www.pi5.uni-stuttgart.de/documents/abgeschlossene-arbeiten/2021-Prochnow-Ole-Setup-of-a-Laser-System-for-Molecular-Laser-Cooling-BSc.pdf

[35] M. R. Tarbutt and T. C. Steimle, *Modeling magneto-optical trapping of CaF molecules*, Physical Review A - Atomic, Molecular, and Optical Physics **92**, 5 (2015), p. 053401,
URL: https://doi.org/10.1103/PhysRevA.92.053401

[36] S. Xu, P. Kaebert, M. Stepanova, T. Poll, M. Siercke and S. Ospelkaus, *Engineering the sub-Doppler force in molecular magneto-optical traps* (2022),
URL: https://doi.org/10.48550/arXiv.2203.07754

[37] A. M. L. Oien, I. T. McKinnie, P. J. Manson, W. J. Sandle and D. M. Warrington, *Cooling mechanisms in the sodium type-II magneto-optical trap*, Phys. Rev. A **55** (1997), pp. 4621–4624,
URL: https://link.aps.org/doi/10.1103/PhysRevA.55.4621

[38] B. E. A. Saleh and M. C. Teich, *Fundamentals of Photonics* (John Wiley & Sons, 1991), ISBN: 9780471358329

[39] H. Kübler, *Anleitung des AP zum Versuch O15: Gauss-Strahlen*, Universität Stuttgart, Physikalisches Praktikum I (2021),
URL: https://www3.physik.uni-stuttgart.de/studium/praktika/ap/pdf_dateien/O15.pdf

[40] I. Moskalev, *Multiwavelength and ultrabroadband solid-state and semiconductor spatially-dispersive lasers*, PhD thesis, University of Alabama (2004), URL: https://www.researchgate.net/publication/253073664

[41] M. Pfeifer, S. Weissmantel and G. Reisse, *Direct laser fabrication of blaze gratings in fused silica*, Applied Physics A: Materials Science and Processing **112** (2013), pp. 61–64, URL: https://doi.org/10.1007/s00339-012-7202-1

[42] R. Paschotta, *Diffraction grating*, RP Photonics (2022), URL: https://www.rp-photonics.com/diffraction_gratings.html

[43] W. Demtröder, *Experimentalphysik 2, Elektrizität und Optik*, vol. 7 (Springer Spektrum Berlin, Heidelberg, 2017), URL: https://doi.org/10.1007/978-3-662-55790-7, ISBN: 9783662557891

[44] R. Paschotta, *Raman Gain*, RP Photonics (2022), URL: https://www.rp-photonics.com/raman_gain.html

[45] N. Seymour-Smith, P. Blythe, M. Keller and W. Lange, *Fast scanning cavity offset lock for laser frequency drift stabilization*, Review of Scientific Instruments **81**, 7 (2010), p. 075109, URL: https://doi.org/10.1063/1.3455830

[46] C. Tomschitz, *A photoionization scheme to create cold ionic impurities from Rydberg atoms*, Master's thesis, University of Stuttgart (2018), URL: https://www.pi5.uni-stuttgart.de/documents/abgeschlossene-arbeiten/2018-Tomschitz-Christian-A-photoionization-scheme-to-create-cold-ionic-impurities-from-Rydberg-atoms-MSC.pdf

[47] *DL pro, Grating Stabilized Diode Laser Head designed for DLC pro (Manual)*, Toptica Photonics AG (2022)

[48] *VRFA-SF-Series User's Manual Raman Fiber Amplifier and Second Harmonic Generator for Amplification of Single Frequency Signals and Frequency Conversion VRFA-SF and VRFA-SF-Plus Series*, MPB Communications Inc. (2022)

[49] *Toptica DL pro 022103 1212 nm (Data sheet)*, Toptica Photonics AG (2021)

[50] *MPB VRFA-P-2000-606-SF (Data sheet)*, MPB Communications Inc. (2021)

[51] *Toptica DL pro 022108 1256 nm (Data sheet)*, Toptica Photonics AG (2021)

[52] *MPB VRFA-P-2000-628-SF (Data sheet)*, MPB Communications Inc. (2021)

[53] *Stabilisierte He-Ne-Laser Serie SL 04 (Test report)*, SIOS Meßtechnik GmbH (2022)

[54] E. Pultinevicius, *Scanning transfer cavity lock (in progress)*, Master's thesis, University of Stuttgart (2022)

[55] A. J. Olson, R. J. Niffenegger and Y. P. Chen, *Optimizing the efficiency of evaporative cooling in optical dipole traps*, Phys. Rev. A **87**, 5 (2013), p. 053613, URL: https://doi.org/10.1103/PhysRevA.87.053613

[56] S. J. M. Kuppens, K. L. Corwin, K. W. Miller, T. E. Chupp and C. E. Wieman, *Loading an optical dipole trap*, Phys. Rev. A **62**, 1 (2000), p. 013406, URL: https://doi.org/10.1103/PhysRevA.62.013406

[57] J.-F. Clément, J.-P. Brantut, M. Robert-de Saint-Vincent, R. A. Nyman, A. Aspect, T. Bourdel and P. Bouyer, *All-optical runaway evaporation to Bose-Einstein condensation*, Phys. Rev. A **79**, 6 (2009), p. 061406, URL: https://doi.org/10.1103/PhysRevA.79.061406

[58] *1064 nm CW Fiber Laser & Amplifier: ALS-IR-1064-50-I-CP-SF (Test report)*, Azurlight Systems (2022)

[59] T. A. Savard, K. M. O'Hara and J. E. Thomas, *Laser-noise-induced heating in far-off resonance optical traps*, Phys. Rev. A **56**, 2 (1997), pp. R1095–R1098, URL: https://doi.org/10.1103/PhysRevA.56.R1095

[60] K. Meyer, *An optical dipole trap for a two-species quantum degenerate gas*, Diploma thesis, University of Heidelberg (2010), URL: https://www.physi.uni-heidelberg.de/Forschung/QD/datafiles/publications/theses/2010_Kristina_Meyer.pdf

[61] F. Tricot, D. H. Phung, M. Lours, S. Guérandel and E. de Clercq, *Power stabilization of a diode laser with an acousto-optic modulator*, Review of Scientific Instruments **89**, 11 (2018), p. 113112, URL: https://doi.org/10.1063/1.5046852

All links were accessed last on August 18, 2022.

Acknowledgments

My bachelor's thesis at the 5th Institute of Physics has been a thoroughly enjoyable experience. Therefore, I would like to thank the following physicists from the institute:

- Dr. Tim Langen, for initiating my fascination with ultracold molecular physics, for the opportunity of doing my bachelor's thesis in the ColdMolecules team and for your expert guidance.
- Prof. Dr. Tilman Pfau, for sparking my interest in optics and atomic physics and for giving me the opportunity to deepen this interest. Thank you, for the possibility to complete my bachelor's thesis at your institute.
- Phillip, for introducing the CaF experiment to me, answering all my questions, your great willingness to help in the laboratory, great support and an overall awesome time in the CaF team.
- Marian, Felix and Einius, for passing on your expertise and creating a very pleasant atmosphere in the ColdMolecules Team.
- All members of the institute, for being there to help with technical problems, having great lunch breaks and enjoying fun activities.

I would also like to thank all my friends and fellow students for the great support during my bachelor's degree and making it so much more fun! Without you this would not have been possible!

Finally, I would like to thank my family, for always supporting and believing in me and for always being on my side.